Preprints (www.preprints.org) | NOT PEER-REVIEWED | Posted: 21 September 2021

Comparison between methods for indirect assessment of buildability in fresh 3D printed mortar and concrete

Irina Ivanova*, Egor Ivaniuk, Sameercharan Bisetti, Venkatesh N. Nerella, Viktor Mechtcherine

Institute of Construction Materials, TU Dresden, 01062 Dresden, Germany

**Corresponding author. Email address: irina.ivanova@tu-dresden.de*

Abstract: This paper presents a comparison between indirect methods for assessing the buildability of 3D printed cementitious materials, including CRV or CSR test using rotational rheometry, unconfined uniaxial compression test (UUCT), a newly proposed confined uniaxial compression test (CUCT), and fast penetration test. The experimental program was conducted on the extruded samples of six printable mortars and two printable concretes with various rheological behavior achieved by the use of different additives and admixtures. Predictions of the material failure and the stability failure in hollow cylindrical structures are provided and compared with the results of the direct printing test. Benefits and disadvantages of the employed test methods are discussed, also taking into consideration a perspective of their use for automated in-situ control of the materials' buildability.

Keywords: *3D concrete printing, digital concrete, layered extrusion, fresh concrete rheology, green strength, buildability, rotational rheometry*

1. Introduction and theoretical background

The past few years in the construction industry are marked by the rapid development of DFC technologies (Digital Fabrication with Concrete) [1], the number and quality of which are constantly growing, enabling numerous advancements including production efficiency [2–5] and customization [1,6,7]. Both industry and scientific communities are working intensively on finding optimal solutions for material design, testing methods, and technical specifications for various manufacturing techniques. The most widespread DFC technologies currently are based on layered extrusion. Belonging to the additive group of approaches in the RILEM classification [1], layered material extrusion is showing great potential for mass housing construction [2,7–10]. It enables erecting formwork-free structures via layer-by-layer material deposition. On the one hand, freshly deposited layers must retain their shape under their own weight and the weight of the subsequently placed layers; on the other hand, the overall structure must be stable without any buckling [2]. The feature which stands for such behavior of fresh 3D printed concrete (3DPC) is usually referred to as "buildability" [2,3,9,11].

1.1 Buildability and its direct assessment

Buildability of 3DPC depends on its rheological properties and is attributable, among others, to yield stress and thixotropy of cementitious materials [2]. Yield stress is defined as a minimal stress required to initiate the flow of a material in the case it was in the static state (static yield stress) or to terminate its flow in the case it was moving (dynamic yield stress) [12,13]. Thixotropy represents a decrease in the apparent viscosity of a fluid over time when this fluid is exposed to shear. Conversely, when a fluid is at rest, its apparent viscosity increases [14]. For cementitious materials, due to their reactive nature, thixotropy depends on the shear history, the age, i.e. time after contact with water, and on some other factors [15,16]. Thus, such materials are capable of not only restoring their structure (due to reflocculation) after removing the applied load, which is described by a parameter "reflocculation

© 2021 by the author(s). Distributed under a Creative Commons CC BY license.

Preprints (www.preprints.org) | NOT PEER-REVIEWED | Posted: 21 September 2021

rate", but also of further structural build-up over time (due to hydration), which is characterized by a parameter "structuration rate", or "structural build-up rate" [4,17,18].

Based on the yield stress and thixotropic behavior of cementitious materials, two main approaches towards mix design of 3DPC exist. The first one assumes designing a material with high initial yield stress and reflocculation rate, and a comparatively low structuration rate. Another approach involves a material with low/moderate initial yield stress, but with a fast structuration rate and quick setting, which is achieved by using fine-tuned ternary binder systems or by adding an accelerator to the Portland cement-based materials directly in the 3D printer's nozzle [2]. A combination of both approaches is also possible, which will be illustrated in this paper.

Various methods are currently in use for assessing the buildability of 3DPC. The most straightforward way is the so-called "*buildability test*" or "*direct printing test*" [3] which commonly includes printing a structure of a certain geometry: a) until it collapses, and measuring the number of layers at collapse as well as noting the type of failure; b) with a predefined amount of layers, and evaluating the level of deformations in the printed element [19]. The time interval between layers can be varied to simulate the rate of their loading by material deposition in the case when a larger structure is produced. However, in buildability tests performed until collapse the time interval is normally minimal. Two most common elements chosen by researchers for buildability tests are straight walls [2,3,20,21] and hollow cylinders [19,22–27]. Sometimes more complex structures are printed, such as hollow walls [21], walls with zigzag shapes inside [28], cones and half-sphere domes [22], etc.

No standard procedure for testing buildability has been established yet and the most printed structures in buildability tests differ in many parameters, e.g., layer geometry, i.e., shape, width, and height, as well as in the ratio between layer width and length of the wall, or in the ratio between layer width and diameter of the hollow cylinder. It should be realized that the print object geometry prominently affects its resistance to failure [2,21,22]. For instance, Wolfs et al. [21] conducted a buildability test of the same material by printing a 1-*m* straight wall, a 5-*m* straight wall, and a rectangular structure with long sides of 5.0 *m* and short sides of 0.2 *m*, which failed at respectively 21-22 layers, 27 layers, and 46 layers. Current studies show that that vertical structures of complex shape, as well as closed structures, exhibit higher stability [2,21]. Bester et al. [22] suggested that self-support, e.g. as in a hollow cylinder, can limit the sensitivity of a structure to geometrical imperfections. They performed experimental and numerical research on the printed objects of different shapes and proposed to apply a vertical hollow cylinder with a cylinder diameter to nozzle diameter ratio of 10, a descending cone, and a half-sphere dome as benchmark structures for 3D concrete printing. Nerella et al. [3] proposed a practice-oriented buildability criterion which involves the evaluation of buildability by printing a scaled-down model of the required structure and determining layer-to-layer time interval based on the economic viability of the target structure. The authors emphasized that the downscaling is limited by the concrete composition and proposed that the minimum dimension of the layer cross-section must be trifold of the maximum aggregate size.

1.2 Material and stability failures

Two main types of collapses are described in the literature for the freshly 3D-printed concrete wall structures, viz. material failure (plastic collapse) and stability failure (buckling). The type of failure depends on the object geometry, loading rate, material properties, and boundary conditions [21]. *Material failure (plastic collapse)* occurs when the compressive load σ_c imposed by the subsequently placed layers exceeds the strength of the printed material in the bottom layer, see Eq. (1):

$$\sigma_c = \rho g h_t \tag{1}$$

where ρ is the density of the printed material, g is the gravitational acceleration constant, and h_t is the height of the printed object. Parameter h_t is time-dependent and equal to the height of a single layer h_0 at the beginning of a printing process when the material should have enough strength to retain the layer's shape under its own weight.

Stability failure (buckling failure) occurs due to local or global instability of the whole 3D-printed structure [21]. The structure must theoretically be stable when Young's modulus is higher than its

Preprints (www.preprints.org) | NOT PEER-REVIEWED | Posted: 21 September 2021

critical value according to Eq. (2) [29]. This equation was first introduced by Greenhill in 1881 to describe the critical height, at which self-buckling of a uniform cylindrical pole must occur.

$$E_c \approx \frac{\rho g A h_t^3}{8I} \tag{2}$$

where ρ is the density of the printed material, g is the gravitational acceleration constant, A is the horizontal cross-sectional area, h_t is the height of the printed structure, and I is the quadratic moment of inertia.

Due to the thixotropy of cementitious materials, both compressive strength and Young's modulus of 3DPC are time-dependent properties. Their time-dependency must be considered when predicting the maximum height of the printed structure at a certain rate of printing.

Further details about buildability analyses considering material failure and/or buckling failure can be found in Perrot et al. [30], Wangler et al. [31] and Roussel et al. [29].

1.3 Indirect methods to assess buildability

Although direct buildability tests are important for understanding the behavior of fresh 3DPC, they are obviously material-, time- and labor-consuming and, hence, they are usually applied to validate the printability of mixtures which are preliminary designed / developed by means of indirect methods [9]. Compression tests such as unconfined uniaxial compression test (UUCT) and squeeze flow test are used more often [18,24,25,32–37]. Other techniques include rotational rheometry [18,32], penetration test [5,35], non-destructive ultrasonic measurements [11,21,38] and triaxial compression test [21].

Unconfined uniaxial compression test (UUCT) enables to determine both compressive strength and Young's modulus of 3DPC at its various ages. Furthermore, the rate at which these parameters evolve over time can be calculated. The measurements are deformation-controlled and performed on cylindrical samples of fresh concrete with the height larger than the diameter. The samples are usually cast with compaction using molds consisting of two semi-cylinders. The sizes of samples vary in different research. Wolfs et al. [24] and Panda et al. [32] used samples with D = 70 *mm*, H = 140 *mm*; Kurt et al. [33] chose the dimensions of D = 75 *mm*, H = 100 *mm*, Reiter [35] – D = 90 *mm*, H = 180 *mm*, and Casagrande [39] – D = 60 *mm*, H = 120 *mm*. It has been reported that the samples must be large enough to eliminate size effects (mostly so-called wall effect) leading to non-uniform particle size distribution across the specimen's cross-section [24], but not too large, so that they adequately represent the dimensional scale of the concrete during the printing process [36]. Most researchers applied the ratio H/D = 2 to allow a diagonal shear failure plane formation [24], which follows the requirements of ASTM D2166 for testing cohesive soil. The sample is loaded with a constant deformation rate which varies in the different research from 0.05 *mm/s* [36] and 0.2 *mm/s* [35] to 0.5 *mm/s* [24,25,36]. Wolfs et al. [24] argued that the deformation rate must be sufficiently high to avoid the effects of thixotropic build-up.

According to the current state of the art, not only cast cylindrical samples can be used in uniaxial compression tests of 3DPC. Jayathilakage et al. [25] proposed to perform a uniaxial compression test on the printed samples, for which they used fragments of a single printed layer with the dimensions of L = 100 *mm*, h_0 = 10 *mm*, and w = 30 *mm*. The upper and the bottom plate in the testing device had the same length and width as the samples. The benefit of this technique is that the measurements are performed on the extruded samples, i.e., on the material in its actual state upon deposition. However, the authors recognized that the sample height was too low to achieve failure in the weakest failure plane and stated that the confining effects from the two compression plates could increase the compression stress significantly. They suggested that the method should not be applied for the determination of the compressive strength but that it is suitable for assessing the evolution of Young's modulus E. However, Bos et al. [11] argued that such an approach could also lead to an overestimation of E due to confinement in the longitudinal direction.

Preprints (www.preprints.org) | NOT PEER-REVIEWED | Posted: 21 September 2021

Unlike UUCT, *squeeze flow tests* are stress-controlled and conducted on the cylindrical samples with the height normally smaller than the diameter. Perrot et al. [18] used samples with D = 60 *mm* and H = 35 *mm*. Each sample was loaded in specific stress increments chosen to simulate the loading steps during 3D printing with a particular time interval between layers; the resulting deformation was recorded. The advantage of this method is that the load can be imposed in simplistic ways: a) by placing a container on top of the sample aligned to its center of gravity and gradually adding sand into it [33], or b) by putting weights on the top plate placed on the sample [37]. In the other known cases when this test was used [18,32], the researchers applied the load by a testing machine.

Another method which is now commonly employed for evaluating fresh concrete's properties in quasi-static conditions is *rotational rheometry*. Constant shear rate (CSR) test, or constant rotational velocity (CRV) test, can be applied to assess the evolution of the static yield stress τ_0 over resting time t_{rest}. In CRV test, a small value of constant rotational velocity is applied to the material at different ages, and the resulting torque is recorded until its peak value (flow onset) is achieved [15]. After calculating τ_0 from the values of maximum torque, the τ_0 (t_{rest}) curve is used to evaluate the structuration rate either by Roussel's linear model [17], see Eq. (3), or by Perrot's exponential model [18], see Eq. (4).

$$\tau_0(t_{rest}) = \tau_0 + A_{thix} \cdot t_{rest} \tag{3}$$

$$\tau_0(t_{rest}) = \tau_0 + A_{thix} \cdot t_c \cdot (e^{t_{rest}/t_c} - 1) \tag{4}$$

where t_{rest} is the resting time; τ_0 is the initial static yield stress at t_{rest} = 0; A_{thix} is the structuration rate; and t_c is the characteristic time, the value of which is adjusted to obtain the best fit with experimental results.

As some of 3DPCs tend to build the structure up very fast due to rapid reflocculation, it can be also important to assess their reflocculation rate by applying the first part of the Kruger's bilinear model, see Eq. (5). According to Kruger et al. [40], taking reflocculation rate into consideration enables higher precision in predicting the ability of the freshly printed layers to retain their shape. The second part of the Kruger's model, see Eq. (6), describes the structuration in 3DPC similarly to the Roussel's model.

$$\tau_0(t_{rest}) = \tau_D + R_{thix} \cdot t_{rest}, \quad t_{rest} \leq t_{rf} \tag{5}$$

$$\tau_0(t_{rest}) = \tau_0 + A_{thix} \cdot (t_{rest} - t_{rf}), \quad t_{rest} > t_{rf} \tag{6}$$

where τ_D is the dynamic yield stress; R_{thix} is the reflocculation rate; t_{rest} is the resting time; t_{rf} is the time period over which reflocculation occurs, or the inflection point of the bilinear model; τ_0 is the initial static yield stress at $t_{rest} = t_{rf}$; A_{thix} is the structuration rate.

The benefit of using rotational rheometry for estimating the properties of fresh 3DPC is that rheometers enable to access both dynamic rheological properties and static rheological properties of the material, also with short time intervals between testing points. However, if the material is too stiff, i.e. its initial yield stress is too high, there is a high probability of reaching the torque limit of the device faster than the maximum t_{rest} of interest is reached [40]. Another drawback of this method is that no precise evaluation of concrete's elastic behavior is accessible due to plug flow [41], especially in the wide-gap rheometers. In this case, measuring the actual strain in the tested sample becomes impossible [15].

There are only a few examples of applying CRV protocol for testing the actual printable mortars in the literature. Perrot et al. [18] used a 4-blade vane rheometer to assess the structural build-up in a fine printable mortar. In each single measurement, a shear rate of 0.001 s^{-1} was applied for 180 *s* after 1 min of pre-shearing. The measurements were conducted for 90 *min* after mixing at each 10 *min*; the probe was taken out in between the tests. Panda et al. [32] used a rotational rheometer with a vane probe for testing the development of the static yield stress in a printable mortar with the maximum aggregate size of 1.2 *mm* by applying a constant shear rate of 0.1 s^{-1} for 60 *s*. The measurements were conducted at the age of 5, 30, 60, 90, and 150 *min*. The authors claimed a good correlation between τ_0 (t_{rest}) and the evolution of compressive strength over time which was determined by UUCT. Benamara et al. [42] measured τ_0 of a fresh printable mortar with the maximum aggregate size of 2

Preprints (www.preprints.org) | NOT PEER-REVIEWED | Posted: 21 September 2021

mm using a rheometer with a vane probe and applying a complex protocol which included pre-shear at a very high shear rate of 600 s^{-1} followed by a CSR measurement at 0.01 s^{-1}. The authors used the obtained results to deduce Young's modulus E from the shear elastic modulus G, assuming that $G = \tau_c/\gamma_c$, where τ_c is the shear stress and γ_c is the shear strain at the end of the linear part of the shear stress – shear strain curve. This approach can be considered approximate, since, as discussed above, no precise measurement of strain in a high yield stress material is possible.

One more promising method for assessing the buildability of 3DPC indirectly is *penetration test*. It was introduced as a technique for evaluating the yield stress of cement pastes by Lootens et al. in [43], where the authors compared the effect of the various shapes of penetrometers, i.e. hemispherical, conical, needle-type, etc., and provided analytical formulas for calculating the yield stress from the measured penetration force. The measurements were performed with a controlled penetration rate of 1 *μm/min*. The methodology was further developed by Reiter [35] who proposed two variations of this approach for evaluating the structural build-up of cement pastes, i.e. fast penetration test and slow penetration test. Fast penetration protocol included testing a sample in multiple points at a rate of 1 *mm/s*, while slow penetration required continuous penetration of a tip in the sample at a rate of 20 *mm/h* over a long period of time. To ensure the accuracy of the obtained yield stress values, the author introduced a depth correction factor for a conical penetrometer. For cement pastes, an excellent agreement between the results of penetration tests, uniaxial compressive strength measurements, and CSR tests was reported. Moreover, Pott et al. [44] concluded a strong correlation between the data from penetration experiments, rheometry, QXRD, and calorimetry for cement pastes. The authors applied the fast penetration method using a conical penetrometer with D = 6 *mm* and the cone angle of 40°; penetration rate equaled 0.7 *mm/s*. Such drawbacks of the fast penetration test as a manual shift of the sample and the necessity to clean the penetration tip after each measurement were noted.

Although the penetration method seems very promising for 3D printed materials, the data on using this technique for characterizing the structural build-up in printable mortars and concretes is still very limited. Reiter [35] provided a comparison between the results of the penetration tests, uniaxial compressive strength measurements, and CSR tests for mortars with 0-2 *mm* crushed limestone aggregates added in the amount of 20, 40, and 48 *%* by volume. In this case, weaker correlations were observed in comparison with those for pastes. The yield stress values estimated by the slow penetration technique were higher than the ones assessed by compression tests, which can be a consequence of demolding and sample transportation. For the slow penetration test, the author has noted that the method is limited to materials with such aggregate fraction that no frictional contacts can appear. It was also recommended to use a penetration tip with a diameter five times larger than the maximum aggregate size. In [40], Pott and Stephan implemented slow penetration test with a spherical penetrometer, D = 7.5 *mm*, for investigating the structural build-up in a printable mortar with a sand-to-binder weigh ratio of 1 and a maximum aggregate size of 0.5 *mm*. The loading rates were 0.072 *mm/min* and 0.005 *mm/min*. The authors reported good reproducibility of the results, however, underlined the increased difficulty of the data analysis for mortars in comparison with pastes. Dressler et al. [45][46] implemented fast penetration test for discontinuous in-situ investigation of the structural build-up in 3D printed shotcrete with the maximum aggregate size of ca. 3 *mm* in the time period from 5 *min* to 90 *min* after the material's deposition. The applied penetrometer had a diameter of 3 *mm*, a cylindrical height of 12.5 *mm*, and a cone height of 2.5 *mm*.

Besides providing good correlations with other methods, penetration technique generally ensures a higher measurement range in terms of the sample's consistency, i.e. from quite soft materials which are not testable with the uniaxial compression method, to rather stiff samples which cannot be assessed by rotational rheometry due to torque limitations of the devices [35]. This feature makes penetration test very promising both at the stage of mix design and for the in-situ control of 3DPC's properties.

Preprints (www.preprints.org) | NOT PEER-REVIEWED | Posted: 21 September 2021

1.4 Ratio between compressive strength and yield stress

Alongside with the challenges of establishing proper testing methods for 3D printable mortars and concretes, the task of predicting their buildability when erecting various structures has not been yet solved. Due to the complexity of load distribution in the freshly printed structures and the thixotropy-induced changes in 3DPC over time, it is still being discussed how the compression stress and the shear stress of the material must be related [11].

Three criteria are usually mentioned in the literature. Initially, Wangler et al. [10] proposed to use the *von Mises plasticity criterion*, see Eq. (7):

$$\tau_0(t) \geq \sigma(t)/\sqrt{3} \tag{7}$$

where $\tau_0(t)$ is a time-dependent yield stress of the printed material, $\sigma(t)$ is its time-dependent compressive stress, and $\sqrt{3}$ is a factor that considers the proportion between the von Mises failure stress in pure shear and uniaxial tension [11].

The same approach was discussed and adopted by different researchers [5,35,42], however, Jacquet et al. [47] criticized the use of the von Mises criterion because of the "asymmetric" resistance of fresh cement-based materials subjected to compressive and tensile stresses. Bos et al. [11] argued that Eq. (7) overestimates the magnitude of the equivalently induced shear stress resulting from a normal load application, hence the material failure is also overvalued.

The *Tresca criterion*, which is based on the assumption of reaching the maximal shear stress at the wall bottom, was considered as another possible approach, see Eq. (8) [4,11,27,35,48,49]:

$$\tau_0(t) \geq \beta \cdot \sigma(t) \text{ with } \beta \leq 0.5 \tag{8}$$

where the factor β is determined by the largest and smallest principal stresses [11].

The Tresca criterion is the lower bound of the *Mohr-Coulomb criterion* [27], see Eq. (9) [24], which is currently considered the most accurate for estimating the buildability of 3D printed mortars, yet requires additional experimental investigations such as direct shear tests [24].

$$\tau_0(t) = C(t) + \sigma_n \cdot \tan\varphi \tag{9}$$

where $C(t)$ is the time-dependent cohesion between particles bonded by cement, σ_n is the acting normal stress, and φ is the angle of internal friction caused by the frictional resistance and interlocking between internal particles. $C(t)$ and φ are established by direct shear tests performed at various ages of the printable mortar.

The cohesion $C(t)$ can be described by a linear [24] or bilinear model [11], depending on the material's structuration rate and the time range under investigation. The angle of internal friction φ shows no clear trend of development over time and a large scatter [11,24], thus, it is considered as time-independent, and the average value is applied. The Mohr-Coulomb failure criterion was implemented in numerous works [11,21,22,24,25,48] and reported to provide the most accurate prediction for buildability of 3D printable mortar up to date.

1.5 Summary and research goals

Since the construction industry is promptly moving towards the automation of construction technologies, automation in the control of 3DPC properties will also soon be required. Even without considering robotization, assessing the elastoplasticity of cementitious materials is not an easy task. It is due to their time-dependent thixotropic behavior, which depends on the shear history, ambient conditions, and other factors affecting the fresh material starting from its mixing and till its setting. In the last years, several methods were proposed for the evaluation of 3DPC's strength performance over time, including direct printing test, unconfined uniaxial compression test (UUCT), squeeze flow test, CRV test (rotational rheometry), and penetration test. All of these techniques have their limitations in terms of admissible consistency of the tested samples and in terms of the parameters which can be determined. No clarity is yet reached in relating compression and shear stresses in the freshly printed structures, which creates additional difficulties in establishing correlations between compressive

Preprints (www.preprints.org) | NOT PEER-REVIEWED | Posted: 21 September 2021

strength on one hand and shear strength or yield stress of 3DPC on the other. The methods also seem to have various levels of complexity in sample preparation and different perspectives with respect to automation. Moreover, few data is available on testing directly the printed samples, especially if they are made of concrete, not of mortar or paste.

This paper focuses on the comparison of various methods for indirect assessment of buildability of fresh 3D printed mortars and concretes, which are promising for being adopted as in-situ tests for automated quality monitoring during the printing process. To perform the comparison, we employed rotational rheometry, UUCT, penetration test, and a newly proposed adaptation of the uniaxial compressive test, which we called confined uniaxial compression test (CUCT). Although UUCT is not a perspective method for the in-situ quality control, it has been the most intensively applied testing protocol up to date, hence in this research, we attempted to upgrade it by conducting experiments on the specimens which were cut out from the printed layers, rather than testing cast samples. Taking into consideration possible effects of the material on the obtained correlations between various testing methods, eight different mixtures were designed for this experimental program in order to gain higher confidence in the quality of the conducted comparison. Direct printing tests were also performed. Using layered extrusion technique, hollow cylindrical structures were printed until they collapsed or reached the maximum height of 40 layers (1.2 *m*). The results of the direct printing tests were compared to the predicted heights of the printed structures which were calculated using the data obtained in the indirect tests.

2. Materials and methods

2.1 Mix design

Six printable mortars and two printable concretes with the maximum aggregate size of 2 *mm* and 8 *mm*, respectively, were designed to perform this research. The binder in all compositions comprised 55 *%* by mass CEM I 42.5 R (HeidelbergCement AG, Germany), 30 *%* fly ash Steament® H-4 (Power Minerals GmbH, Germany), and 15 % microsilica powder 971U (Elkem Silicons Germany GmbH). Quartz sand of fractions 0.06–0.2 *mm*, 0–1 *mm*, 0–2 *mm*, 2–4 *mm*, and gravel of fraction 4–8 *mm* were used as aggregates. Aggregate composition for all printable mortars comprised 20 *%* of volume fractions 0.06–0.2 *mm*, 20 *%* 0–1 *mm*, and 60 *%* 0–2 *mm*; for printable concretes the portions of aggregate fractions were 16 *%* 0.06–0.2 *mm*, 16 *%* 0–1 *mm*, 43 *%* 0–2 *mm*, 13 *%* 2–4 *mm*, and 12 *%* 4–8 *mm*. The volume fraction of aggregates in the mortar mixtures was 46.5–47.7 *%*, and 50.3–51.4 *%* in the concrete mixtures.

Experimental PCE superplasticizer VP 2018/14.1 (MBCC Group, Germany) was added to all compositions to ensure the required rheological properties at moderate water-to-binder ratios (w/b). One mortar and one concrete were designed with no extra admixtures (except for PCE superplasticizer) and are labeled as “NA”. Composition 2-NA was based on the recipe developed by Nerella [50]. Five other mortars contained various additives or admixtures, i.e. 0.75 *%* by volume of steel fiber with hooked ends, L = 25 *mm*, D = 0.4 *mm*, produced by KrampeHarex GmbH & Co. KG., Germany (printable mortar 2-StF0.75); 0.5 vol*%* of polypropylene fiber Dyneema®, L = 6 *mm* (printable mortar 2-PF0.5); 0.1 *%* (by weight of dry mix) of clay-based viscosity modifying agent Acti-Gel® 208 supplied by Faber&VanderEnde BV, Germany (printable mortar 2-Clay0.1); 0.*1 %* (by weight of dry mix) of cellulose ether Tylose MH 300 P2 supplied by SE Tylose GmbH & Co. KG, Germany (printable mortar 2-CE0.1); and 4 *%* (by weight of binder) of accelerator Master X-Ceed 120 produced by MBCC Group, Germany (printable mortar 2-Acc4). The second concrete composition 8-CA comprised a complex admixture including 0.05 *%* (by weight of dry mix) of Acti-Gel® 208 and the same dosage of Tylose MH 300 P2, as well as 3 *%* (by weight of binder) of accelerator Master X-Ceed 120.

Compositions of printable mortars and concretes as well as their basic properties are given in Table 1. The workability of mixtures was tested on the extruded samples by the Hägermann flow table (HFT) test in accordance with EN 1015-3 [51]. The density of fresh mortar/concrete was determined according to EN 12350-6:2019 [52].

Preprints (www.preprints.org) | NOT PEER-REVIEWED | Posted: 21 September 2021

Table 1. Compositions and parameters of printable mortars and concretes.

Composition		**2-NA**	**2-StF0.75**	**2-PF0.5**	**2-Clay0.1**	**2-CE0.1**	**2-Acc4**	**8-NA**	**8-CA**
Component		***Amount per 1 m³ [kg]***							
Binder	CEM I 42.5 R	393	392	388	390	360	392	389	362
	Fly ash	214	214	212	209	197	214	198	193
	Microsilica powder	107	107	106	106	98	107	100	98
Aggregate	Sand 0.06–0.2 *mm*	253	253	250	252	250	253	219	214
	Sand 0–1 *mm*	253	253	250	252	250	253	219	214
	Sand 0–2 *mm*	759	741	750	755	751	758	581	569
	Sand 2–4 *mm*							177	173
	Gravel 4–8 *mm*							168	164
Additive, admixture	Superplasticizer	9.7	9.7	10.5	9.6	9.3	7.7	9.4	9.5
	Steel fiber		60.0						
	PP fiber			5.0					
	Clay-based VMA				2.0				1.0
	Cellulose ether					1.9			1.0
	Accelerator						28.5		19.6
	Water	246	246	249	251	271	224	221	225
Property		***Value***							
Spread by HFT [*mm*]		151	148	149	148	129	139	146	125
Density [*kg/m³*]		2144	2228	2169	2181	2005	2155	2227	2217

2.2 Experimental program and specimen production

A total amount of 165 *L* of each mixture was prepared for a single test sequence. Since the highest volume of mixer available in our laboratory was 60 *L*, three batches of the material were prepared one after another and then homogenized in a 200-*L* container. Individual batches were prepared in a single-shaft Ammann 60-*L* ELBA mixer, the total mixing time equaled 10 *min*. Homogenization of the unified batch was done via a portable dual paddle concrete mixer for 5 *min*. The material was also systematically remixed every 10 *min* during the entire printing process in order to reduce the effect of reflocculation on the rheological properties and hence avoiding problems with unstable extrudability. The unification procedure could be adopted only because of the relatively long setting time of the binder under investigation. In the case of accelerated compositions, the unification procedure was excluded, and mortar/concrete was mixed upon the need for more printing material. The accelerator was added at the last stage of mixing, 4 to 5 *min* before the material was fed to the hopper of the 3D printer.

All tests were performed on the samples of extruded mortar/concrete, so that the structure of the material stays as close as possible to its actual state after deposition by a 3D printer. It should be especially relevant for compositions containing fiber due to its predominant orientation in the direction of printing [53,54]. The overview of the experimental program for assessing the buildability of printable mortar/concrete is presented in Table 2. Each testing method will be discussed in detail in further sections. Fig. 1 shows a schematic representation of indirect testing methods including unconfined uniaxial compression test (UUCT), confined uniaxial compression test (CUCT), and penetration test (PT). The widths of the specimens for CUCT and PT are not featured in Table 2 and Fig. 1, as they were variable due to the applied printer nozzle, see Section 2.3 for more details.

Preprints (www.preprints.org) | NOT PEER-REVIEWED | Posted: 21 September 2021

Table 2. Overview of experimental program for assessing buildability of printable mortar/concrete.

Method	Output parameters	Samples	Application for compositions:							
			2-NA	2-StF0.75	2-PF0.5	2-Clay0.1	2-CE0.1	2-Acc4	8-NA	8-CA
Direct printing test	Number of layers at collapse	Hollow cylinders: R = 200 *mm*, h_0 = 30 *mm*	✓	✓	✓	✓	✓	✓	✓	✓
Rheometry (CRV test)	τ_D; τ_S; R_{thix}; t_{rf}	3 *L* (= cell capacity)	✓	✓	✓	✓	✓	✓	✓	✓
	τ_0; A_{thix}		✓		✓	✓			✓	
Unconfined Uniaxial Compression Test (UUCT)	σ_{max}; $\dot{\sigma}_{max}$	Cylinders: D = 49 *mm*, H ≈ 50 *mm*	✓			✓	✓	✓	✓	✓
Confined Uniaxial Compression Test (CUCT)	σ_{max}; $\dot{\sigma}_{max}$; E; $\dot{E}$	2 subsequently printed layers: h = 60 *mm*, L ≈ 250 *mm*	✓	✓	✓	✓	✓	✓	✓	✓
Penetration test (PT)	τ_0; $\dot{\tau}_0$	2 subsequently printed layers: h = 60 *mm*, L ≈ 150 *mm*	✓	✓	✓	✓	✓	✓		

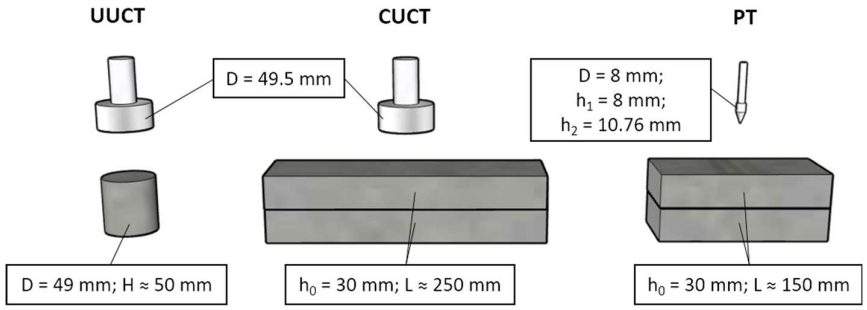

Fig. 1. Indirect methods for assessing buildability.

To produce the samples, two layers were subsequently printed with the minimal time interval on the support material covered with rigid plastic plates. For UUCT and PT, the plates had a square shape with an edge length of 150 *mm*; for CUCT – rectangular shape and the size of 100 × 250 *mm*. Deposited layers were promptly removed from the printing area, cut with a trowel into individual samples, and stored under a thin plastic film to prevent extra water evaporation from the specimen's surface. The laboratory conditions during the whole set of experiments were in the following range: temperature of 17-22 *°C*, relative humidity of 40-50 *%*. The samples for UUCT were further cut out from the fragments of two printed layers using a thin steel hollow cylindrical mold with a sharp bottom edge; the mold dimensions were D = 50 *mm*, H = 50 *mm*. For mixtures with fiber, this technique was not sufficient to produce cylindrical samples of good quality. As fiber predominantly aligns in the direction of printing, cutting through the printed layer becomes difficult and, most importantly, it changes the fiber alignment. For this reason, there will be no results of UUCT presented for the mortars 2-StF0.75 and 2-PF0.5. The data on the penetration measurements for concrete mixtures will not be given, since the penetration tip used in this research was designed for pastes and mortars, had a diameter of 8 mm and, hence, was too small for testing materials containing 8-*mm* aggregates [35].

For each mix, all comparative tests were conducted on the samples from the same unified batch, with a similar shear history and at the same resting times of 0, 20, 40, 60, and 80 *min* (and 0, 15, 35, and 55 *min* for the printable mortar 2-Acc4 due to its faster structuration). The printing process in the direct printing tests also started at the resting time of 0 *min*. Unfortunately, it was not possible to keep the material ages, at which the tests were started, equal for all of the investigated compositions. This was due to variations in the time required for selecting a proper rotational velocity of the extruder. For this reason, the effects of various additives and admixtures on the buildability of mortars and concretes will not be an object of an in-depth discussion in this paper.

Preprints (www.preprints.org) | NOT PEER-REVIEWED | Posted: 21 September 2021

2.3 Direct printing test (buildability test)

In each direct printing test, a hollow cylindrical structure with the radius R = 200 *mm* and the layer thickness h_0 = 30 *mm* was produced. The radius in this case is defined as the distance between the center of the cylinder to the center of the printer nozzle. Each printed layer had a joint; the joins of two subsequently printed layers were placed on the opposite sides. This printing technique is not conventional and was used to additionally assess the cohesiveness of the printed material which is a part of another research.

A laboratory-scale 3D concrete printer with a printing area of approximately 1.4 *m* x 1.0 *m* was used. The maximum printing height is ca. 1.2 *m*, which provided the possibility to print a cylinder with a maximum number of layers equal to 40. The hopper of the printhead has a 50-*L* capacity and is equipped with steel blades which feed the material to the extruder. The extruder is a screw pump with the screw diameter of 110 *mm* and the channel depth of 280 *mm*. A circular vertically oriented nozzle with an outlet diameter of 60 *mm* was used in the present research. The printing process was handled with a constant printing rate of 50 *mm/s*. The rotational velocity of the extruder depended on the properties of the material and was adjusted shortly before the printing process started. As the printer nozzle had no side trowels restricting the material's flow, the layer width was variable for different printed compositions. Also due to its dependency on the rheological properties of mortar/concrete, in the case of pauses while printing the accelerated compositions, a portable concrete vibrator had to be used for breaking the structure of the material inside of the printer and enabling its flow. The structure was printed until collapse or until its total height reached 40 layers. The printing process was documented using a video camera, so that the exact moment of collapse and the failure mode could further be evaluated.

The laboratory-scale 3D concrete printer incl. its particular parts and a sample of the hollow cylindrical structure during its printing process are presented in Fig. 2.

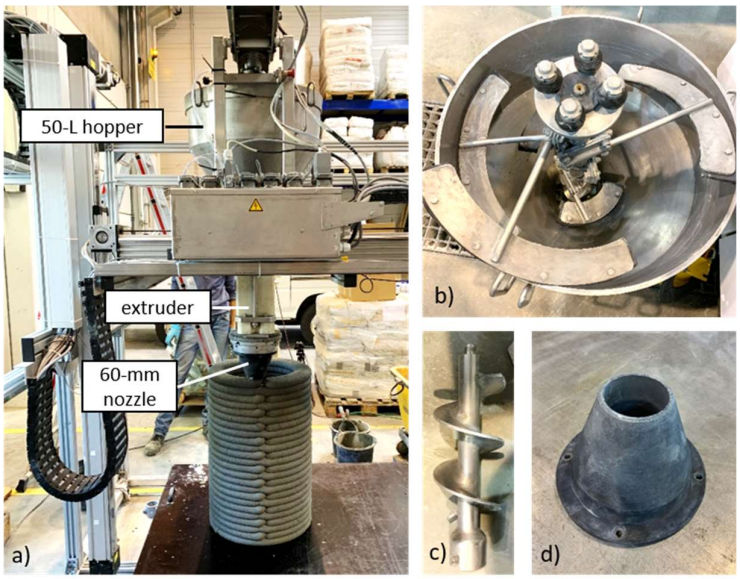

Fig. 2. (a) Laboratory-scale 3D-printer with (b) a hopper equipped with rotating steel blades, (c) a screw extruder (here: screw only), and (d) a 60-*mm* circular nozzle.

2.4 Constant rotational velocity (CRV) test

CRV test is done by means of rotational rheometry and includes determination of the peak values of torque at a low constant rotational velocity applied to the sample of a cementitious material at selected ages or resting times. In this research, we used a dual-head, Couette-type rheometer Viskomat XL (Schleibinger Geräte Teubert und Greim GmbH, Germany) equipped with a ribbed cell with a height of 170 *mm* and an inner diameter of 135 *mm* and with a six-blade vane probe; the height

Preprints (www.preprints.org) | NOT PEER-REVIEWED | Posted: 21 September 2021

of the blades is 69 *mm*, the diameter is 69 *mm*. The applied constant rotational velocity was 0.3 *rpm*. The single-batch approach was followed, i.e. all measurements of the peak torque at various resting times were conducted on the single sample of the material [15]. Static yield stress measurements were conducted at the resting times of 0, 1, 2, 3, 5, 10, 15, 20, and each 20 *min* further on, until the torque limit of 5000 *N·mm* (approximately equals 10 *kPa*) was reached. The sample was manually sheared right before the first measurement. Such a procedure was designed in order to be able to assess the dynamic yield stress, reflocculation time, and reflocculation rate as parameters of the Kruger's model [48]. When assessing these parameters, the testing protocol must be designed with very short time intervals between measurements in the first few minutes of the test, and the sample must be sheared right before starting the test to break the material's structure. Manual shearing was preferred to shearing of the material by the rheometer itself, because this way it can be done in the whole volume of the sample, and no plug is formed. Plug formation was anticipated due to the high yield stress of the material, and it could negatively affect the results of the subsequent static yield stress measurements leading to an underestimation of the material's resistance to shear. The very first, "zero" measurement of the peak torque was excluded from the analysis; it was only required for proper rotor positioning in the sample before starting the main tests [15]. The step duration for the next measurement at t_{rest} = 1 *min* was 3 *s*; this was required to achieve the equilibrium torque after the peak [48]. For further measurements, a step duration of 1 *s* was chosen to prevent excessive disturbance of the sample, i.e. each measurement was broken off as soon as possible after the peak value of torque was reached [15]. A sample of raw data plots obtained with the described protocol is given in Fig. 3a.

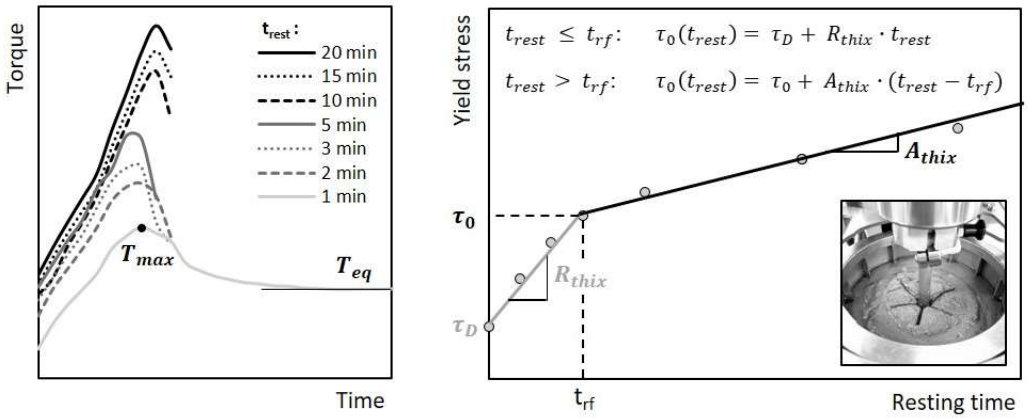

Fig. 3. CRV test (rotational rheometry): (a) raw data plots at different resting times, (b) data analysis according to the Kruger's model.

The measurements were performed at room temperature, i.e. without using a cooling module, so that the conditions could be comparable to those for printed mortar or concrete. It is important to note that, for every individual measurement, it must be ensured that the peak torque was followed by a plateau or by a drop in torque values. If the peak torque was reached only at the end of the step, its value is underestimated and must be excluded from the analysis.

To calculate yield stress τ, both dynamic and static, from the measured values of torque T, Eq. (10) was applied:

$$\tau = \frac{T}{2r^2\pi h} \tag{10}$$

where r and h are the radius and the height of the probe, respectively. For the dynamic yield stress τ_D, torque T was equilibrium torque T_{eq} (see Fig. 3a) found as an average of the last ten values. For the static yield stress τ_0, T was equal to the maximum measured value of torque T_{max}.

Preprints (www.preprints.org) | NOT PEER-REVIEWED | Posted: 21 September 2021

All data points were plotted as dynamic/static yield stress versus resting time. Inflection point on the graph, whenever present, was defined as reflocculation time t_{rf}. For resting time less or equal to t_{rf}, reflocculation rate R_{thix} was determined in accordance with the Kruger's model, see Eq. (5); τ_0 was considered equal to the static yield stress at t_{rf}. The structuration rate A_{thix} was evaluated according to Eq. (6). An example of data analysis is given in Fig. 3b.

2.5 Unconfined uniaxial compression test (UUCT)

Unconfined uniaxial compression test was performed using the cylindrical samples with D = 49 *mm* and H ≈ 50 *mm* which were cut out from two subsequently printed layers using a metal hollow cylinder with a thin wall. As discussed in Section 1.3, UUCT is normally conducted on the samples with H/D ≈ 2. However, while this is easily achievable for cast specimens, cutting such specimens out of the extruded material without significant deformation of the latter wouldn't be a simple task. Thus, H/D ≈ 1 was applied. The number of specimens tested at each resting time was three, hence 15 specimens in total were prepared for each mixture under investigation.

The production of the specimens started right after the layers were printed and was performed in the shortest possible timeframe; 1-2 *min* per sample was required. The samples were visually inspected for defects and uniformity of shape; the samples of poor quality were excluded from the investigation. After the production, each specimen was placed under a plastic container to prevent excessive evaporation of water from its surface. The samples were tested in the same order as they were produced.

Testing machine Zwick 1445 with a 50-*kN* load cell was used for conducting compression tests. The diameter of the upper loading plate was equal to 49.5 *mm*. The constant loading rate of 0.5 *mm/s* was applied. Time, force, and deformation were recorded. Each test was carried out until the vertical deformation of 12 *mm* was reached; the testing time including positioning the samples between the loading plates equaled 2-3 *min*. The testing sequence was video-recorded, so that the lateral deformations could be assessed by means of image analysis in the open-source software ImageJ. To calculate the compressive strength σ_{max} of the material at different resting times, the maximum force values were determined. An example of the force-deformation curves obtained in UUCT as well as the typical appearance of the samples before and after testing, depending on their failure mode, are presented in Fig. 4.

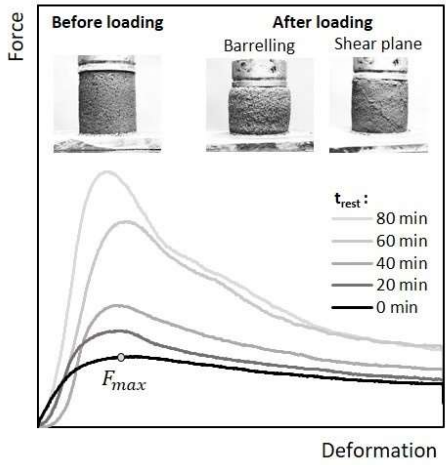

Fig. 4. UUCT: example of force-deformation curves at various resting times and typical failure modes.

Although, unlike in the majority of experiments done by other scientists, the ratio between the specimen's diameter and height was approximately equal to 1, the failure patterns observed in this research were similar to those previously reported. In most cases, barrelling of samples was detected; at later ages or for compositions with higher compressive strength, a clear shear plane failure was also obtained.

Preprints (www.preprints.org) | NOT PEER-REVIEWED | Posted: 21 September 2021

Two approaches for the data analysis were employed and compared: a) considering lateral deformations in the sample and recalculating its cross-sectional area for determination of the compressive strength; b) determination of the compressive strength by applying the initial cross-sectional area of the sample.

The resultant value of the compressive strength was taken as the average of three values if the difference between each individual value in the series and their average was less or equal to 10 *%*. In the case this condition was not met, the average of two closest values, the difference between which was less or equal to 10 *%*, was calculated and accepted as the final result. If such an average could not be established, the measurement was considered unsuccessful, and the correspondent data point was excluded from further analysis. Such an approach was used to prevent the obviously erroneous data points from affecting the quality of correlations between the results obtained by various testing methods.

While obtaining the maximum values of force and the diameter of a specimen at the time of failure was uncomplicated, difficulties were faced when approaching the determination of Young's modulus. For numerous samples, the linear part on the stress-strain curves could not be well defined due to their pronounced curvature. This led to a significant scatter in the results, thus, Young's modulus was excluded from the comparison.

2.6 Confined Uniaxial Compression Test (CUCT)

Confined uniaxial compression test is an attempt to perform uniaxial compressive measurements directly on the printed layers, similar to the test employed by Jayathilakage et al. [25] for the determination of Young's modulus. Although this approach seems less scientific in comparison with the other testing practices applied in this research, it shows promise as a quick, simple, and field-oriented quality control method, which can also be automated and conducted simultaneously with a 3D printing process. Unlike in [25], in the current research CUCT was performed on the segments of not one, but two subsequently printed layers. The total height of each segment was 60 mm and the length equaled 250 *mm*. One sample per one resting time was prepared and then tested in three spots.

The testing device, setting parameters, and principle of calculating the resultant values were kept the same as for UUCT, see Section 2.5. Since considering the lateral deformations in the sample was not feasible in this case, determination of the compressive strength was done by applying the diameter of the upper loading plate (49.5 *mm*) for calculating the cross-sectional area.

Unlike in UUCT, no issues were faced in the determination of Young's modulus. Two approaches for its calculation were adopted. The first one included manual analysis of the graphs with the determination of the size of a linear region on the force-deformation curves, the values of compressive strength and strain, and further calculation of the resultant E. Application of this method helped to establish the ratio between the force at the end of the linear segment and the maximum force, as well as to estimate the typical range of deformations for the tested compositions. Since the main idea of using CUCT is moving toward automation of quality control for 3D printable concrete, the second approach enabled automatic data analysis according to the procedure summarized in Fig. 5.

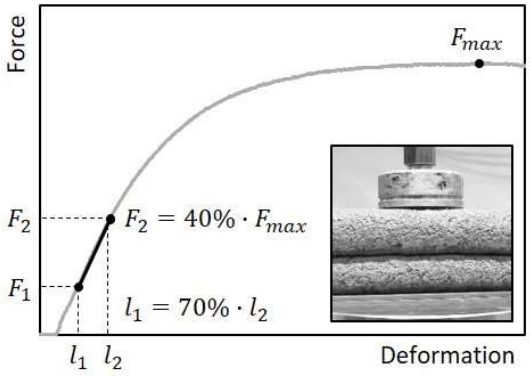

Fig. 5. CUCT: pattern for automated calculation of Young's modulus.

Preprints (www.preprints.org) | NOT PEER-REVIEWED | Posted: 21 September 2021

To perform the required calculations, the following steps must be followed:

- Finding the maximum value of the force F_{max}.
- Calculating F_2 which equals 40 % of the maximum force. According to the graphic analysis (first approach) performed for 120 graphs (8 compositions tested at 5 ages, 3 repetitions per age), the ratio of 40 % ensures that the force-deformation curve below this value is linear for the investigated compositions.
- Finding the value of deformation l_2 corresponding to F_2.
- Calculating 70 % of this deformation value, thus finding l_1. This step is required due to imperfections in the initial section of the force-deformation curve which are caused by the uneven surface of the tested sample or by a small gap between the specimen's surface and the loading plate at the beginning of the measurement; an example of the latter can be observed in Fig. 5. When testing in an automatic regime, such imperfections are inevitable and must be taken into account in further calculations. The ratio of 70 % was chosen based on the results of the graphic analysis.
- Finding the force F_1 which is attributable to l_1.
- Calculating the slope of the force-deformation curve in the established range. The value of Young's modulus is further determined using the cross-sectional area of the upper loading plate and the height of the tested sample. A trivial linearity check of the force-deformation curve in the range under consideration was performed; the coefficient of determination was controlled and expected to be equal to or higher than 0.98. Otherwise, the data point was excluded from further analysis.

The results obtained with the first and the second approachs were further compared. For this test, all calculations were carried out in a standard office program MS Excel. This indicates the simplicity of data processing and its availability for the general user.

2.7 Penetration test

Penetration test was conducted on the segments of two subsequently printed layers with a total height of 60 *mm* and a length of 150 *mm*. A conical penetrometer with a diameter of 8 *mm* and a cone height of 10.78 *mm*, connected to a cylinder with a height of 8 *mm* was applied. The penetrometer movements were controlled by a testing machine ZwickRoell with a 50-*N* load cell. The tests were done using the fast penetration approach with the loading rate of 0.5 *mm/s* until the penetration depth of 19 *mm* was reached, which corresponded to the full immersion of the penetrator in the sample. Time, penetration force, and penetration depth were recorded. At each resting time, a single sample was tested in three points with at least a 3-*cm* distance between them. After taking each measurement, the penetrometer was cleaned with a wet cloth and then treated with a dry cloth. Due to the cleaning procedure, a single measurement sequence required ca. 3 *min*.

A typical penetration force vs. penetration depth curve recorded in the penetration test of a 3D-printed mortar is presented in Fig. 6.

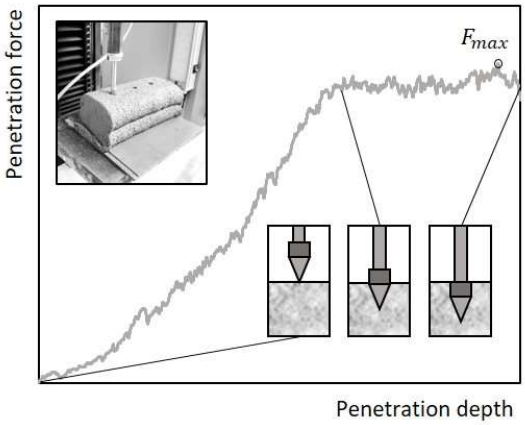

Fig. 6. Penetration test: a typical penetration force vs. penetration depth curve and correspondent levels of the penetrator's immersion into the sample.

Preprints (www.preprints.org) | NOT PEER-REVIEWED | Posted: 21 September 2021

Initially, the penetration force is growing from the moment when the tip starts penetrating the sample and till the moment when the conical part of the penetrator reaches full immersion. From that point, either a plateau (in most cases) or a peak (at later ages and for the mortars with faster structuration) can be observed. In some cases, the curve does not reach a peak or a plateau, then the measurement is excluded from the analysis because the true value of the penetration force remains unknown. Such results can be attributable to the local agglomeration of the aggregate particles or fibers, which causes prominent frictional contacts.

In accordance with Lootens et al. [43], the static yield stress τ_0 was calculated using Eq. (11):

$$\tau_0 = \frac{F}{\pi R(\sqrt{R^2 + h_2^2} + 2h)} \tag{11}$$

where F is the maximum penetration force within the penetration depth of 19 *mm*, R is the cone radius, h_2 is the cone height, and h is the height of the connected cylinder. In this investigation, τ_0 [*kPa*] = 2.897 · F [*N*].

For calculating the resultant value of τ_0 from the three individual data points, the same principle as described for the determination of the resultant value of the compressive strength in UUCT was followed, see Section 2.5.

3. Results and discussion

3.1 Results of the direct printing test

The results of the direct printing test are presented in Table 3.

Table 3. Results of direct printing test.

	2-NA	2-StF0.75	2-PF0.5	2-Clay0.1	2-CE0.1	2-Acc4	8-NA	8-CA
Rotational velocity of the extruder [*deg/s*]	50	75	110	73	50	110	80	60
Layer width [*mm*]	80	80	90	88	65	92	80	62
Duration of printing [*min*]	23	27	17	26	30	33	34	35
Number of layers at collapse [-]	28	27	23	31	34	> 40	33	> 40

As mentioned in Section 2, the printing rate was set at 50 *mm/s*, while the rotational velocity of the extruder varied depending on the material's extrudability. Due to using a circular nozzle in the printing process, the layer width was also a variable affected by the properties of the applied composition. The actual duration of printing was not exactly as estimated based on the geometry of the printed structure and on the printing rate. This is due to the extra time which was occasionally required for refilling the hopper or for other operations during printing. While the calculated time required for printing a single layer was ca. 0.5 *min*, the actual average value of this parameter equaled 0.9 *min*. The latter value will be used in further calculations when predicting the buildability of the printed structures. The number of printed layers at collapse differed depending on the mixture. Fig. 7 presents the photographs of the printed hollow cylindrical structures either at the moment of their collapse or at the full printing height of 40 layers (1.2 *m*).

The structures printed with accelerated compositions 2-Acc4 and 8-CA reached the maximum height without collapse, while the use of other mixtures resulted in collapse at 23 to 34 layers. For all of the printed samples, the failure mode was not easy to define and is probably a combination of the material failure and the defects in the printed structure. The weakest points leading to these defects were created by the joints of lower quality, i.e. too wide and with uneven edges, which was attributable to the rheological properties of the material. This issue occurred when using mixtures characterized by high cohesiveness of the printed filament such as 2-StF0.75, 2-PF0.5, and 2-CE0.1. It should be noted that for printing with the accelerated compositions, in which the accelerator was added at the last stage of mixing, i.e. not to the printhead, it is extremely important to carefully choose the admixture dosage for a particular structure. Batch size and printing rate should also be taken into account. Otherwise extrudability issues and, as a result, lower quality of the printed filaments, can be observed;

Preprints (www.preprints.org) | NOT PEER-REVIEWED | Posted: 21 September 2021

see sample 2-Acc4 in Fig. 7. For 2-Acc4, a clear difference can be seen between layers produced with older material (midsection) and fresher material (bottom and top sections of the printed cylinder). For 8-CA, the dosage of the accelerator was decreased which resulted in the uniform quality of the structure.

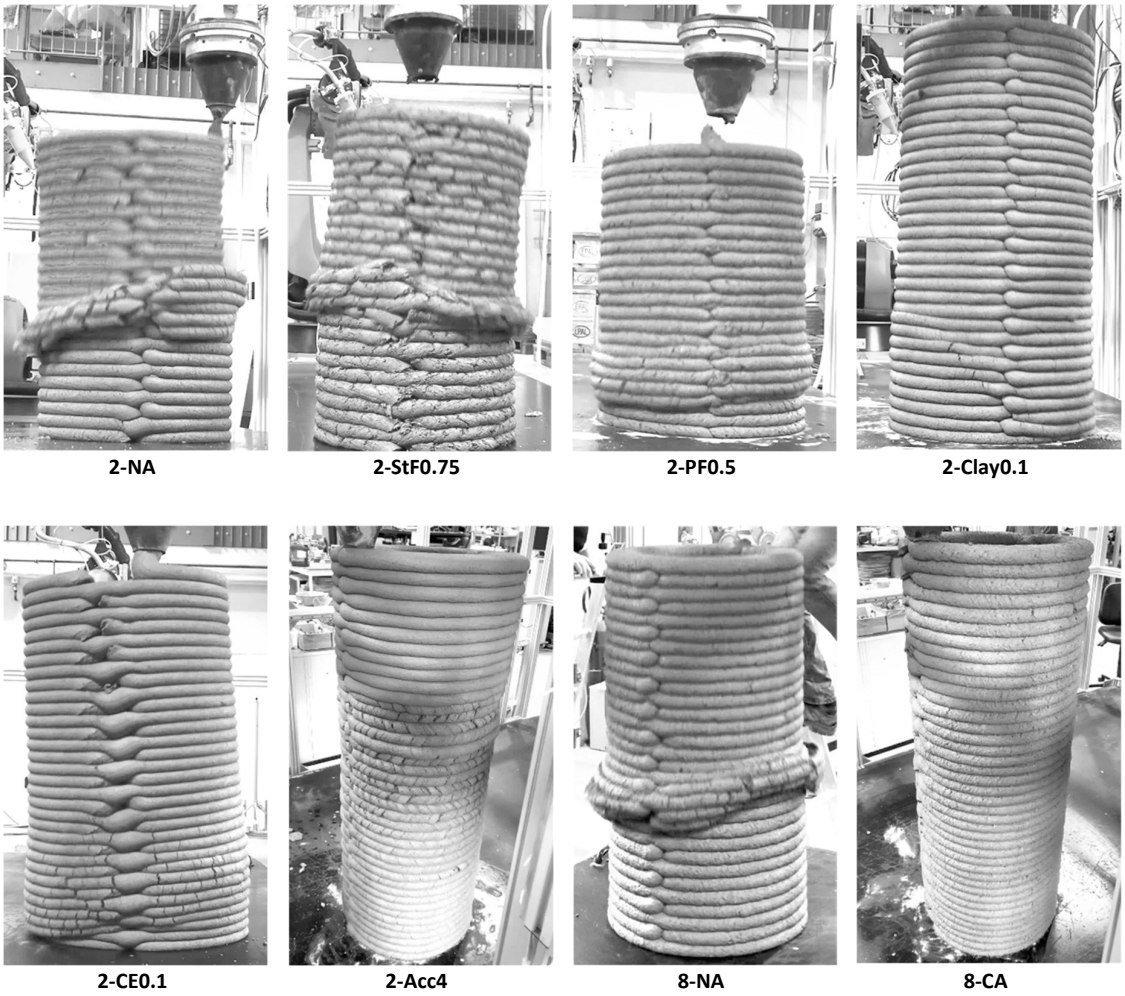

Fig. 7. Printed structures at full printing height (2-Acc4 and 8-CA) or at collapse (other compositions).

3.2 Results of the indirect tests

Experimental results obtained in the indirect tests for assessing the buildability of 3D printable mortars and concretes, including individual values of the compressive strength and the static yield stress at different resting times, as well as the results of some intermediate calculations are given in Tables A.1 and A.2 of the Appendix.

Table 4 provides the parameters of the Kruger's model [48] including dynamic yield stress τ_D, reflocculation rate R_{thix}, reflocculation time t_{rf}, initial static yield stress τ_0, and structuration rate A_{thix} determined by means of the CRV test; the initial compressive strength σ_{max} and its growth rate $\dot{\sigma}_{max}$ measured via UUCT and CUCT; and, finally, the initial static yield stress τ_0 with its growth rate $\dot{\tau}_0$ assessed by the penetration test. CUCT results also include the initial Young's modulus E along with its growth rate $\dot{E}$. All values of the growth rates were calculated for the linear sections of the obtained curves σ_{max} (t_{rest}), τ_0 (t_{rest}), and E (t_{rest}). In UUCT, the initial compressive strength and its growth rate were calculated with consideration of lateral deformations in the samples ("real") and without such consideration ("appr."), see Section 2.5. In CUCT, the initial Young's modulus and its growth rate

Preprints (www.preprints.org) | NOT PEER-REVIEWED | Posted: 21 September 2021

were determined both graphically ("graph.") and by using automatic calculation method ("calc."), see Section 2.6. "PD%" represents the percentage difference between the values resulted from two approaches.

Table 4. Results of indirect assessment of the buildability in the printed mortars and concretes.

	Parameter		2-NA	2-StF0.75	2-PF0.5	2-Clay0.1	2-CE0.1	2-Acc4	8-NA	8-CA
CRV test	τ_D [*kPa*]		2.92	2.95	2.87	3.15	3.79	5.90	3.07	5.19
	R_{thix} [*kPa/min*]		0.62	1.05	0.51	0.64	0.94	1.94	0.79	1.14
	t_{rf} [*min*]		5	3	5	5	3	< 1	5	2
	τ_0 [*kPa*]		6.01	6.10	5.43	6.36	6.59	7.84	7.04	7.46
	A_{thix} [*kPa/min*]		0.12	-	0.12	0.08	-	-	0.18	-
UUCT	σ_{max} [*kPa*]	*real*	11.25	-	-	7.35	10.50	23.34	6.65	30.85
		appr.	12.48	-	-	8.13	14.16	22.79	7.02	36.50
		PD%	*10%*	-	-	*10%*	*30%*	*2%*	*5%*	*17%*
	$\dot{\sigma}_{max}$ [*kPa/min*]	*real*	0.34	-	-	0.17	0.11	0.85	0.10	0.45
		appr.	0.31	-	-	0.22	0.13	0.99	0.12	0.49
		PD%	*9%*	-	-	*23%*	*12%*	*15%*	*16%*	*8%*
CUCT	σ_{max} [*kPa*]		11.11	25.49	17.76	18.75	23.05	47.81	20.20	52.87
	$\dot{\sigma}_{max}$ [*kPa/min*]		0.43	0.47	0.38	0.46	0.24	2.48	0.32	1.46
	E [*MPa*]	*graph.*	1.10	1.74	0.38	0.48	0.46	1.31	0.66	1.05
		calc.	0.98	1.76	0.37	0.48	0.46	1.27	0.68	1.03
		PD%	*12%*	*1%*	*2%*	*1%*	*1%*	*3%*	*2%*	*1%*
	$\dot{E}$ [*MPa/min*]	*graph.*	0.026	0.025	0.008	0.016	0.006	0.064	0.013	0.026
		calc.	0.026	0.025	0.009	0.016	0.006	0.068	0.013	0.028
		PD%	*2%*	*2%*	*12%*	*5%*	*3%*	*6%*	*3%*	*8%*
PT	τ_0 [*kPa*]		4.10	9.33	5.33	5.99	5.07	11.73	-	-
	$\dot{\tau}_0$ [*kPa/min*]		0.10	0.10	0.12	0.13	0.06	0.79	-	-

Since all measured parameters for all compositions increased linearly within the duration the printing process (17-35 *min*), the rate of their growth was characterized by linear models. The Kruger's model is given in Eq. (5) and Eq. (6). The models for calculating $\dot{\sigma}_{max}$, $\dot{E}$ and $\dot{\tau}_0$ are provided in Eq. (12), Eq. (13) and Eq. (14), respectively.

$$\sigma_{max}(t_{rest}) = \sigma_{max} + \dot{\sigma}_{max} \cdot t_{rest} \quad (12)$$

$$E(t_{rest}) = E + \dot{E} \cdot t_{rest} \quad (13)$$

$$\tau_0(t_{rest}) = \tau_0 + \dot{\tau}_0 \cdot t_{rest} \quad (14)$$

Plots depicting structuration in the printed samples of the mortars and concretes are given in Fig. 8 and contain the development of the static yield stress assessed by the CRV test (see Fig. 8a) and penetration test (see Fig. 8d), as well as the development of the compressive strength determined by means of unconfined uniaxial compression test (see Fig. 8b) and confined uniaxial compression test (see Fig. 8c). For the CRV test, in which the material was sheared before testing in order to determine its reflocculation behavior, the values of τ_0 are plotted versus the resting time, for other tests – versus the unification time, i.e. the time, at which mixing of several batches into a single batch was finished. This approach enables a rough comparison of structuration in the different materials.

In the CRV test performed for the accelerated compositions 2-Acc4 and 8-CA, extremely high τ_D of over 5 *kPa* as well as high reflocculation rates (1.94 and 1.14 *kPa/min*, respectively) were detected, thus only a few measurements could be taken before the torque limitation of the device was reached. In the case of 2-Acc4 this took less than 1 *min*. Such fast reflocculation resulted in the necessity for using a portable vibrator in the hopper and sometimes at the nozzle after the material was not sheared for even a short time, otherwise, the printing process was not possible. Compositions 2-CE0.1 and 2-StF0.75 were also characterized by fast reflocculation with R_{thix} of 0.94 and 1.05 *kPa/min*, respectively; however, the use of external vibration was not required. It allows to conclude that, while fast reflocculation rate can generally be considered as a positive quality of a 3D printable material used

for layered extrusion due to its contribution to maintaining the filament's shape right after deposition, it can also provide a negative effect on the printing process when its value becomes too high.

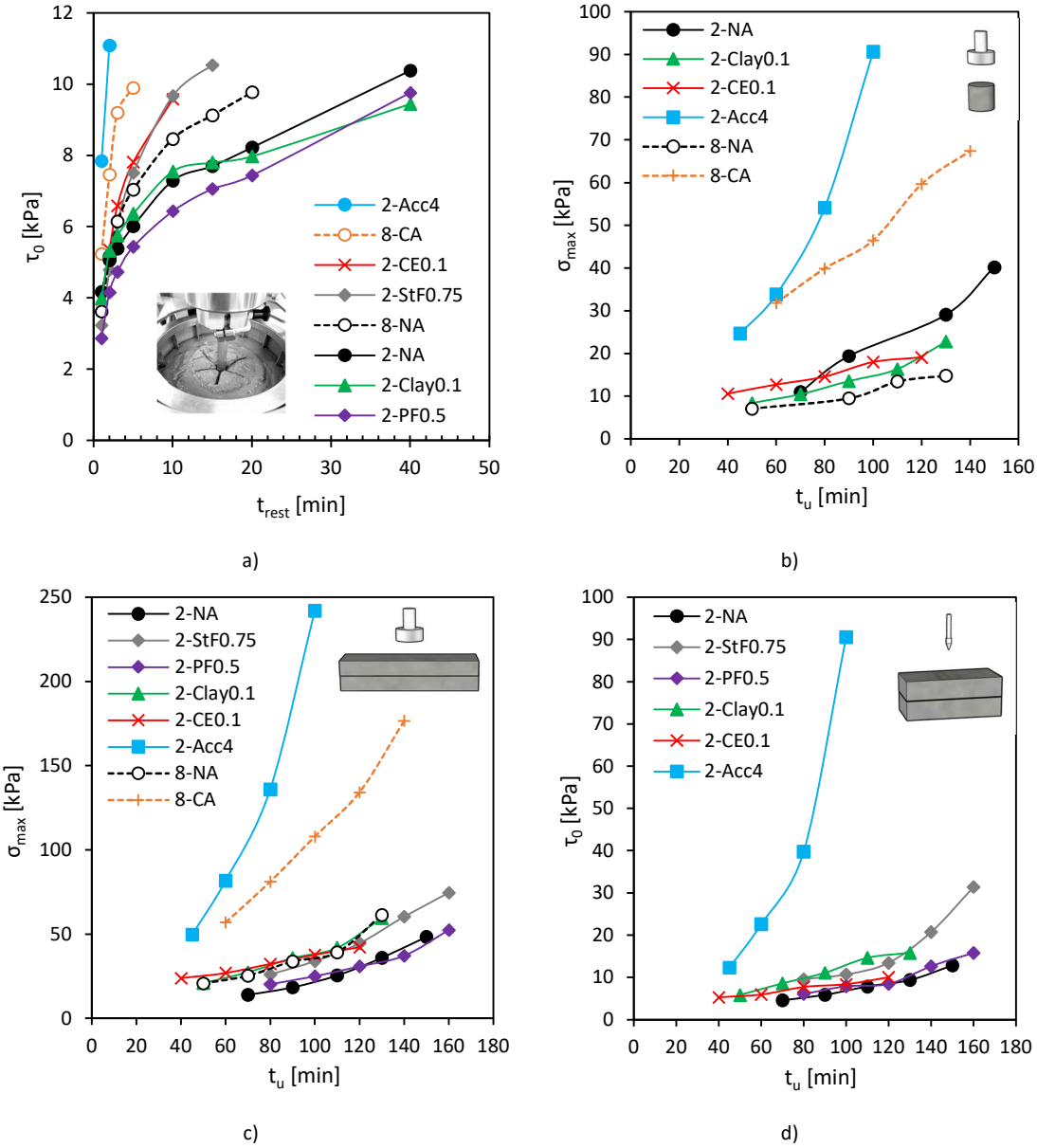

Fig. 8. Structuration in the printed mortars and concretes assessed by means of (a) CRV test, (b) UUCT, (c) CUCT, and (d) penetration test.

When comparing the rheological behavior of compositions with no additional admixtures but different aggregate sizes, it was observed that the initial dynamic yield stress and the reflocculation rate of concrete 8-NA were higher than of mortar 2-NA. The same trend is valid for their structuration parameters τ_0 and A_{thix}. Clay-based VMA did not notably affect the reflocculation behavior of the printed mortar, while the use of polymer fiber led to a slight reduction in both τ_D and R_{thi} . At the same time, the structuration rates of 2-PF0.5 and 2-NA were equal.

It is to be noted that the number of data points for half of the tested compositions was not enough to determine the structuration rate A_{thi} and, consequently, an accurate calculation of the predicted number of layers at collapse will not be feasible for these compositions. Also, due to the difference in the shear history of the material before testing, the results of CRV test will not be compared with the results obtained by compression and penetration tests.

When juxtaposing the data from the other experiments, we can conclude that the results attained in CUCT and in penetration test yield more similar trends than the plots which resulted from UUCT in comparison to CUCT. For instance, while mortar 2-NA shows the slowest structuration in CUCT, in UUCT it exhibits faster strength evolution when compared to 2-Clay0.1, 2-CE0.1, and 8-NA. At the same time, accelerated mixtures 2-Acc4 and 8-CA show a similarly fast increase in σ_{max} in both tests. Such discrepancy can be caused by the difference in the sample preparation for UUCT which included an extra step of cutting the cylindrical specimens from the printed layers. This procedure was time-consuming and imposed an additional shear load on the material before its testing.

In Table 4, the values of the compressive strength σ_{max} evaluated by UUCT are given for two calculation methods. "Real" means that σ_{max} was determined under consideration of the lateral deformations in the sample and with correspondent recalculation of its cross-section, and "appr." is an approximated assessment of σ_{max}, in which the initial cross-sectional area was applied. The percentage difference *PD%* between the values obtained by both calculation approaches shows that the effect of the lateral deformations on the compressive strength is material-dependent. While for compositions 2-NA and 2-Acc4 very similar results could be observed and thus the image analysis can be disregarded, the mortar 2-CE0.1 deformed so significantly that the increase in its cross-section must be considered. Neglecting of the lateral deformations generally led to overestimation of the compressive strength and its growth rate.

When investigating the elasticity in CUCT, the values of Young's modulus E determined by graphic analysis ("graph.") and automatically calculated using the slope of a particular linear segment of the force-deformation curve ("calc."), see Section 2.6, were compared. No significant difference in the results obtained with both approaches was observed. Consequently, the proposed method for automatic calculation of E can be considered valid for the compositions under investigation.

3.3 Comparison between UUCT, CUCT and penetration test

One of the major objectives of this research is to find correlations between the parameters obtained with different indirect methods for assessing the buildability of mortars and concretes. Since in this research UUCT, CUCT, and penetration test were conducted on the samples from the same batch and simultaneously, i.e. at the same resting times, the resultant data points can be directly compared. Fig. 9 shows strong linear correlations between individual values of compressive strength determined with UUCT and CUCT, and the values of static yield stress evaluated by the penetration test.

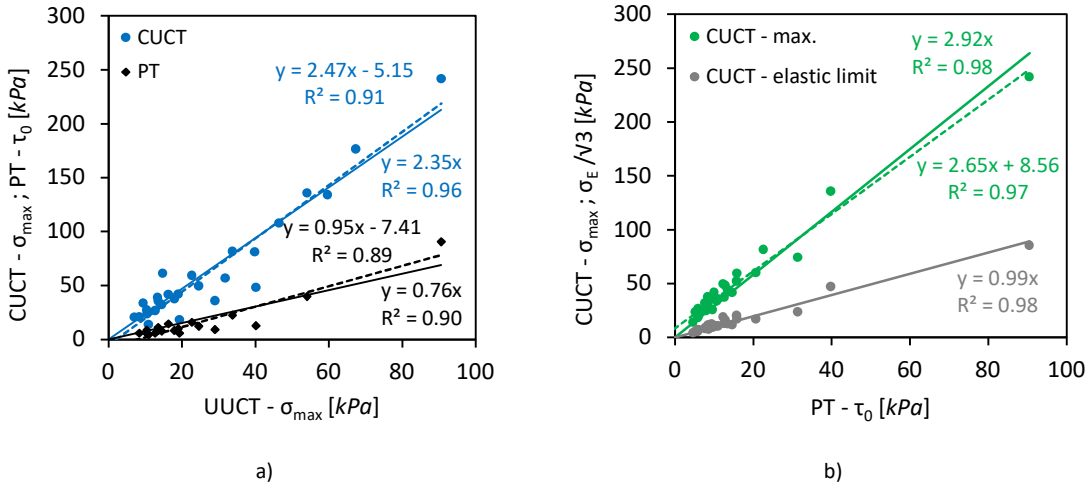

a) b)

Fig. 9. Correlations between the values of the compressive strength and the static yield stress obtained with various test methods: (a) UUCT vs. CUCT and PT, (b) PT vs. CUCT.

The results of UUCT when compared with the data obtained with CUCT and PT showed higher scatter, which is probably due to the differences in the sample preparation, as was discussed in Section 3.2. CUCT provided approximately 2.4 higher values of compressive strength σ_{max} than UUCT due to

Preprints (www.preprints.org) | NOT PEER-REVIEWED | Posted: 21 September 2021

the confined conditions in the longitudinal direction. The correlation between the values of the compressive strength σ_{max} (CUCT) and the static yield stress τ_0 (PT) was of higher precision.

Since all of the established correlations could be, with some level of approximation, drawn through the origin, we can try to apply the Tresca criterion, see Eq. (8), for characterizing the relationship between τ_0 and σ_{max}. In the case of UUCT, coefficient β prominently depended on the tested composition. Its average value was equal to 0.34 for mixture 2-NA, 0.50 for 2-CE0.1, and 0.79 for 2-Clay0.1. Unlike for other compositions, for mixture 2-Acc4 it also significantly varied over the resting time, starting from 0.50 for t_{rest} = 0 *min* and ending up equal to 1.00 at t_{rest} = 55 *min* (see Table A.2 in Appendix for more details). In the case of CUCT, the value of β was much less material-dependent, its average value for all tested compositions equaled 0.3. According to [11], the value of β must be less or equal to 0.5. This condition is met by the results of CUCT and only partially by the results of UUCT.

In the process of data analysis, an interesting observation was made on the relation between the values of the static yield stress τ_0 determined in the penetration test and the values of compressive strength at the elastic limit σ_E that resulted from CUCT. Compressive strength at elastic limit was assessed for calculating Young's modulus and is defined by the force at the end of the linear segment of the force-deformation curve. It was established that in the case when we apply σ_E instead of σ_{max}, the relation between the static yield stress and the compressive strength can be described by the von Mises criterion, see Eq. (15):

$$\tau_0(t) \approx \sigma_E(t)/\sqrt{3} \tag{15}$$

The corresponding correlation between τ_0 and $\sigma_E/\sqrt{3}$ is shown in Fig. 9b; it is characterized with the conversion factor of 0.99 and the coefficient of determination R^2 equal to 0.96. It is also worthwhile noting that the ratio σ_E/σ_{max} was material-dependent, but did not prominently change over resting time for the tested mixtures; see Table A.2 in Appendix. The average values of σ_E/σ_{max} varied from 0.43 for the softer material 2-CE0.1 to 0.63-0.64 for more rigid materials 2-Acc4 and 2-PF0.5. The low time-dependency of this ratio allows to apply the σ_E/σ_{max} established for the zero resting time for estimating the approximate values of σ_E at later ages of the material.

3.4 Predicting the failure of the printed structure

The final target of all discussed testing methods is to be able to predict the height of a particular structure which can be erected using a material of known properties, with a certain printing rate and a time interval between the subsequent layers, without experiencing collapse or major deformations.

Fig. 10 shows the comparison between the number of layers at collapse determined in the direct printing test, and the predicted amount of layers at collapse calculated using the results of CRV test (rotational rheometry), UUCT, CUCT, and penetration test (PT). Using the CUCT results, the number of layers at collapse was calculated for three cases: 1) prediction of material failure using the values of compressive strength σ_{max}; 2) prediction of stability failure based on the values of Young's modulus E; 3) prediction of material failure using the values of compressive strength at elastic limit σ_E.

To assess the material failure, Eq. (1) was applied. For relating the static yield stress resulted from the CRV test (rotational rheometry) and the penetration test to the compressive strength, two approaches were used: 1) the von Mises criterion, as proposed by Wangler et al. [10] and Roussel [29]; see Eq. (7); 2) the geometric factor $\alpha = \sigma/\tau_0$ calculated for a hollow cylindrical structure using the equations found by Weng et al. [23].

If we consider linear growth of the material's strength over the resting time, the number of layers at collapse N_c can be predicted by Eq. (16) and Eq. (17):

$$N_c = \sigma/(\rho g h_0 - \dot{\sigma} t_l) \tag{16}$$

$$N_c = \tau_0/(\rho g h_0/\sqrt{3} - \dot{\tau}_0 t_l) \tag{17}$$

where σ and τ_0 are the initial compressive strength and static yield stress, respectively; $\dot{\sigma}$ and $\dot{\tau}_0$ are the rates of their increase over the resting time; ρ is the density of the printed material; g is the gravitational acceleration constant; h_0 is the height of a single layer, and t_l is the time interval between subsequently printed layers. t_l corresponds to the resting time as t_{rest}/N_c, and the height of the

Preprints (www.preprints.org) | NOT PEER-REVIEWED | Posted: 21 September 2021

printed object relates to the height of a single layer as $h_t = h_0 N_c$. For the printed structure, h_0 = 30 *mm* and $t_l \approx 0.9$ *min*.

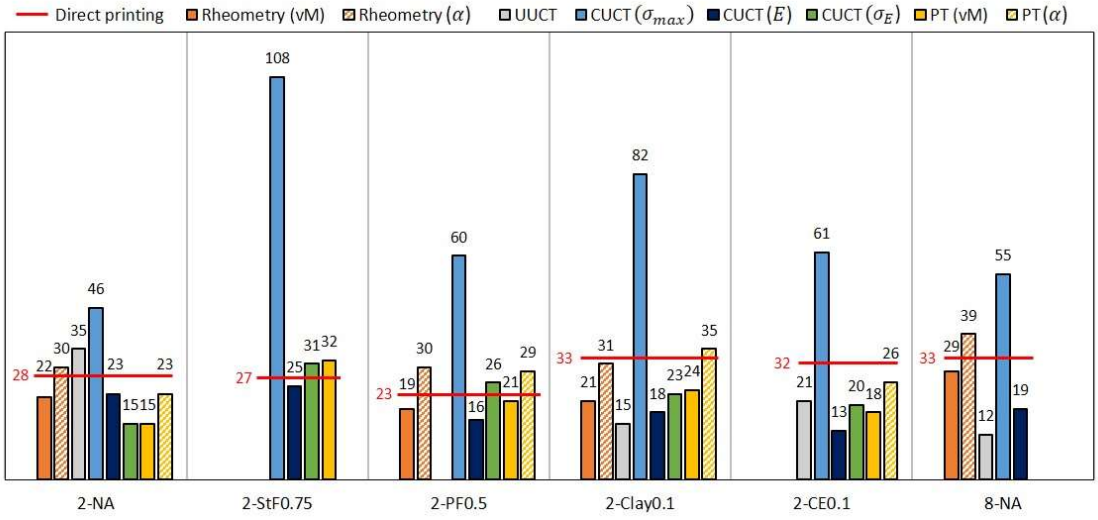

Fig. 10. The number of layers at collapse obtained in the direct printing methods and predicted using the experimental results of the CRV test (rheometry), UUCT, CUCT, and PT. "vM" means the von Mises criterion.

When geometric factor α is introduced, its dependency on the current height of the printed object must be taken into account, hence N_c is determined as an intercept between the critical and the actual static yield stress as a function of the object height expressed in the number of layers.

In the case of rotational rheometry, only a few compositions could be considered in the comparison due to the restricted amount of data caused by the torque limitation of the testing device. However, we can estimate that at the height of 40 layers, which was the maximum printing height, the yield stress of the material in the bottom layer must exceed 13.6 to 15.1 kPa, depending on the density of the material, in order to avoid plastic collapse. According to the very fast structuration of the accelerated mixtures 2-Acc4 and 8-CA (see Fig. 8a), we could assume that the structure printed to its maximum height would not collapse within the printing time of 33-35 min (see Table 3), which corresponds to the experimental observations. However, for compositions 2-CE0.1 and 2-StF0.75 no similar assumptions could be made due to uncertainty in the further trend of τ_0 development over the resting time. Moreover, we can expect that the predicted values of N_c are underestimated to some extent due to intensive shearing of the sample at the beginning of the rheological measurements. As observed in Fig. 10, all predicted values of N_c were indeed lower than in the actual printed structures as soon as the von Mises criterion was used to relate the compressive strength and the static yield stress. Application of the geometric factor α resulted in the improved accuracy of the buildability prediction for compositions 2-NA and 2-Clay0.1, while for compositions 2-PF0.5 and 8-NA it became slightly less precise.

When comparing predictions of the material failure based on the results of UUCT, CUCT, and PT, the following conclusions can be drawn.

- Calculations based on the evolution of the maximum compressive strength assessed by UUCT provided very poor prediction, with overestimation of the material's capacity for composition 2-NA and its underestimation for the other mixtures.
- Using the values of the maximum compressive strength determined in CUCT led to a significant overestimation of the number of layers at collapse for all compositions under investigation.
- The number of layers at collapse, which was calculated from the evolution of the static yield stress obtained in the penetration test using the von Mises criterion and from the evolution of the compressive strength at the elastic limit determined in CUCT, are closely comparable. Both methods provided good predictions for the printability of mortars with fiber 2-StF0.75 and 2-PF0.5. For other cases, the forecast underestimated the actual number of layers in the structure at

Preprints (www.preprints.org) | NOT PEER-REVIEWED | Posted: 21 September 2021

collapse. Application of the geometric factor α in the calculations led to higher prediction accuracy of the penetration test for all compositions except 2-PF0.5.

Stability-failure prediction in Fig. 10 was conducted presuming that the printed object is a straight vertical wall, similar to Roussel's calculations in [29] for the analogous case. If a structure is a straight vertical wall, the general Eq. (2) transforms into Eq. (18), as $A = w$, and $I = w^3/12$:

$$E_c \approx \frac{3\rho g h_t^3}{2w^2} \tag{18}$$

where ρ is the density of the printed material, g is the gravitational acceleration constant, h_t is the height of the printed structure, and w is the layer width.

As in [29], the number of layers at collapse N_c was found graphically as an intersection point between the evolution of the experimentally measured Young's modulus E and the development of required E_c, both as functions of the number of printed layers. However, for the cylindrical structures produced in this research, their approximation into a straight wall led to an underestimation of their actual stability in most cases, as can be concluded from the comparison of the predicted failure and the actual failure in Fig. 10.

If we perform calculations for a hollow cylinder, then $A = \pi(d_o^2 - d_i^2)/4$ and $I = \pi(d_o^4 - d_i^4)/64$, where d_o and d_i are the outer and the inner diameters of the cylinder, thus the general Eq. (2) transforms into Eq. (19).

$$E_c \approx \frac{2\rho g h_t^3}{d_o^2 + d_i^2} \tag{19}$$

As a result, for a 40-layer hollow cylinder to be stable, Young's modulus of the printed material must not be higher than 0.21-0.23 MPa only, which is considerably below any initial value of E for all tested compositions; see Table 4. It means that none of the printed structures should have faced buckling failure. This prediction holds true, as no clear buckling failure was observed in any of the performed direct printing tests.

As a final conclusion, no indirect testing method under investigation has provided a consistently accurate assessment of the number of the layers which can be printed before the structure collapses. This inaccuracy could be caused by various factors including the effects of the printing process (e.g. printer vibration and additional pressure due to vertical extrusion; see [55]), unanticipated defects in the printed structures, imperfections in the experimental procedures, and imprecision of the selected failure criteria for the investigated case. According to the comparison of the predicted and the actual amount of layers at collapse, it can make sense to base the prediction of material failure neither on the maximum compressive strength which overestimates the material's load bearing capacity, nor on the compressive strength at the elastic limit which underestimates it, but rather on some value in-between that will correspond to the admissible level of deformations. A certain strain in the printed layers can be allowed, however, it must be taken into account that the closer the stress approaches the maximum compressive strength, the more unstable the printed structure becomes.

A simpler and probably more efficient way of reducing the problem of plastic collapse and buckling failure due to the insufficient rheological performance of the printed material would be by means of material design, i.e. by using mortars and concretes with a fast-setting binder, which has already been discussed by numerous scientists [2,9,35]. In the current research, using the accelerated mortar and concrete resulted in no collapse of the erected structures even despite the defects in them, because the lower layers had already been set when the upper ones were printed.

4. Conclusions and outlook

In this investigation, a comparison between various methods for assessing the buildability of 3D printed mortars and concretes was conducted. Eight mixtures with different rheological behavior were tested by means of the direct printing test, as well as using indirect methods, i.e. CRV test (rotational

Preprints (www.preprints.org) | NOT PEER-REVIEWED | Posted: 21 September 2021

rheometry), unconfined uniaxial compression test (UUCT), confined uniaxial compression test (CUCT), and penetration test. All experiments were performed on the extruded samples.

Although strong linear correlations between the results of the indirect tests were observed, no consistently accurate prediction of the material failure was obtained with any of the methods. Additionally, some methods had certain limitations in the framework of the experimental program. The use of rotational rheometry was restricted due to the torque limitation of the device, which is also valid for most of the existing rheometers. The prediction for the material failure resulting from the CRV test underestimated the actual capacities of the 3D printable compositions, but still provided a good prognosis, which can further be improved if shearing the sample prior to its testing is excluded. Moreover, it can be possible to employ a torquemeter instead of the rheometer, which will also potentially simplify field testing of 3D printed concrete.

UUCT performed on the samples which were cut out from the two subsequently printed layers with the ratio H/D ≈ 1 enabled determination of the compressive strength over the resting time, but not of Young's modulus. Possibly, samples with higher H/D were required for such assessment. UUCT was labor- and time-consuming, provided the largest scatter in the results, showed little promise for field application, and was not appropriate for the fiber-reinforced mortars due to low quality of the cut-out samples and disruption of fiber alignment.

A newly proposed CUCT method was implemented directly on the printed layers and has shown approximately 2.4 times higher values of the compressive strength in comparison with UUCT. CUCT enabled full investigation of time-dependent elastoplasticity in all printed mortars and concretes and was easy to perform, including the data processing. Its results on the compressive strength of the material at elastic limit $\sigma_E(t)$ could be well correlated to the static yield stress $\tau_0(t)$ determined in the fast penetration test by applying the von Mises criterion, i.e. $\tau_0(t) \approx \sigma_E(t)/\sqrt{3}$. In comparison to CUCT, the penetration test was more difficult to conduct due to the need for cleaning and drying of the penetrometer after each individual measurement. Potential automation of this step can be complicated.

It must be noted that the values of the static yield stress obtained by rotational rheometry and penetration test, as well as of the compressive strength at elastic limit assessed by CUCT provided similar predictions for the material failure in the printed structures, which were underpredictions in most cases. Conversely, the prognosis based on the maximum compressive strength resulting from CUCT has prominently overestimated the buildability of all tested compositions. Thus, we assume that a more precise prediction of buildability can be achieved by using the values of strength in between the elastic limit and the plastic collapse, which are attributable to the admissible level of strain in the material. Further research is needed to specify this recommendation.

Declaration of interests

The authors declare that they have no known competing financial interests or personal relationships that could have appeared to influence the work reported in this paper.

Acknowledgement

This work is a portion of I. Ivanova's PhD research and a part of the project funded by the Deutsche Forschungsgemeinschaft (DFG, German Research Foundation), Project Number 387152958, within the priority program SPP 2005 "OPUS FLUIDUM FUTURUM – Rheology of reactive, multiscale, multiphase construction materials". Furthermore, a part of this work was performed in the framework of the priority program SPP 2187 "Adaptive modularized constructions made in a flux: precise and rapid building", Project Number 424057211.

The authors gratefully acknowledge the funding by DFG, and the support of HeidelbergCement AG for providing the Portland cement, Master Builders Solutions Deutschland GmbH (MBCC Group) for providing the superplasticizer, Faber&VanderEnde BV for supplying the admixture Acti-Gel® 208, and SE Tylose GmbH & Co. KG for the samples of cellulose ether.

Preprints (www.preprints.org) | NOT PEER-REVIEWED | Posted: 21 September 2021

Appendix – Supplementary material

Table A.1. Individual values of the static yield stress resulted from the CRV test (rotational rheometry) at various resting times. Underlined are the values of τ_0 at t_{rf}.

t_{rest} [min]	Static yield stress τ_0 [kPa]							
	2-NA	**2-StF0.75**	**2-PF0.5**	**2-Clay0.1**	**2-CE0.1**	**2-Acc4**	**8-NA**	**8-CA**
1	4.17	3.24	2.87	3.99	3.95	7.84	3.62	5.24
2	5.06	4.78	4.16	5.33	5.35	11.08	5.16	7.46
3	5.39	6.10	4.73	5.76	6.59		6.15	9.19
5	6.01	7.51	5.43	6.36	7.81		7.04	9.90
10	7.30	9.67	6.43	7.55	9.58		8.46	
15	7.70	10.54	7.06	7.80			9.13	
20	8.22		7.43	7.97			9.77	
40	10.38		9.76	9.44				

Table A.2. Individual values of the compressive strength, Young's modulus and static yield stress at various resting times obtained with UUCT, CUCT and penetration test, and calculated parameters

Mixture	t_u [min]	t_{rest} [min]	**UUCT**			**CUCT**						**PT**	**Calculated parameters**			
			σ_{max} [kPa]		**PD%**	σ_{max} [kPa]	σ_E [kPa]	σ_E/σ_{max}	E [MPa]		**PD%**	τ_0 [kPa]	$\sigma_E/\sqrt{3}$ [kPa]	**PD%***	β	
			appr.	*real*					*graph.*	*calc.*					*UUCT*	*CUCT*
2-NA	70	0	11.46	10.94	*5%*	13.96	7.24	0.52	1.13	1.14	*1%*	4.59	4.18	9%	0.42	0.33
	90	20	19.81	19.35	*2%*	18.30	9.78	0.53	1.45	1.41	*3%*	5.86	5.65	4%	0.30	0.32
	110	40				25.42	16.03	0.63	2.17	1.99	*9%*	7.84	9.25	17%		0.31
	130	60	32.00	29.07	*10%*	35.91	22.16	0.62	2.94	2.31	*24%*	9.35	12.79	31%	0.32	0.26
	150	80	36.53	40.17	*10%*	48.34	28.23	0.58	2.96	3.32	*11%*	12.84	16.30	24%	0.32	0.27
								μ = 0.58							**μ = 0.34**	**μ = 0.30**
								RSD = 8%							**RSD = 14%**	**RSD = 10%**
2-StF0.75	80	0				25.94	16.86	0.65	1.83	1.90	*4%*	9.60	9.74	1%		0.37
	100	20				33.90	18.55	0.55	2.05	1.96	*4%*	10.70	10.71	0%		0.32
	120	40				44.56	21.95	0.49	2.82	2.95	*4%*	13.44	12.67	6%		0.30
	140	60				60.28	29.51	0.49	3.33	3.17	*5%*	20.71	17.04	19%		0.34
	160	80				74.49	41.44	0.56	3.71	3.77	*1%*	31.36	23.93	27%		0.42
								μ = 0.55								**μ = 0.35**
								RSD = 11%								**RSD = 12%**
2-PF0.5	80	0				20.15	12.69	0.63	0.40	0.43	*7%*	6.07	7.32	19%		0.30
	100	20				24.96	15.99	0.64	0.54	0.53	*1%*	7.89	9.23	16%		0.32
	120	40				30.79	19.82	0.64	0.68	0.70	*4%*	8.44	11.44	30%		0.27
	140	60				37.13	22.46	0.61	0.74	0.82	*9%*	12.64	12.97	3%		0.34
	160	80				52.35	35.44	0.68	1.07	1.20	*12%*	15.80	20.46	26%		0.30
								μ = 0.64								**μ = 0.31**
								RSD = 4%								**RSD = 7%**

Preprints (www.preprints.org) | NOT PEER-REVIEWED | Posted: 21 September 2021

Mixture	t_u [min]	t_{rest} [min]	UUCT			CUCT						PT	Calculated parameters			
			σ_{max} [kPa]		PD%	σ_{max} [kPa]	σ_E [kPa]	σ_E/σ_{max}	E [MPa]		PD%	τ_0 [kPa]	$\sigma_E/\sqrt{3}$ [kPa]	PD%*	β	
			appr.	*real*					*graph.*	*calc.*					*UUCT*	*CUCT*
2-Clay0.1	50	0	9.48	8.37	*12%*	20.94	12.30	0.59	0.54	0.56	*3%*	5.83	7.10	20%	0.70	0.28
	70	20	12.98	10.44	*22%*	27.35	13.39	0.49	0.76	0.75	*1%*	8.60	7.73	11%	0.82	0.31
	90	40	14.76	13.51	*9%*	35.73	18.57	0.52	1.00	1.05	*5%*	11.07	10.72	3%	0.82	0.31
	110	60	18.43	16.31	*12%*	41.81	20.44	0.49	1.45	1.49	*3%*	14.63	11.80	21%	0.90	0.35
	130	80	28.53	22.75	*23%*	59.48	29.84	0.50	1.76	1.83	*4%*	15.81	17.23	9%	0.70	0.27
								μ = 0.52							**μ = 0.79**	**μ = 0.30**
								RSD = 7%							**RSD = 10%**	**RSD = 10%**
2-CE0.1	40	0	14.60	10.55	*32%*	23.78	10.05	0.42	0.51	0.49	*3%*	5.26	5.80	10%	0.50	0.22
	60	20	16.11	12.69	*24%*	26.89	11.52	0.43	0.51	0.54	*5%*	5.95	6.65	11%	0.47	0.22
	80	40	18.75	14.54	*25%*	32.26	14.42	0.45	0.66	0.66	*0%*	7.73	8.33	7%	0.53	0.24
	100	60	22.59	17.98	*23%*	37.69	16.97	0.45	0.81	0.80	*0%*	8.39	9.80	15%	0.47	0.22
	120	80	23.93	19.06	*23%*	42.14	17.45	0.41	0.94	0.92	*2%*	10.03	10.08	0%	0.53	0.24
								μ = 0.43							**μ = 0.50**	**μ = 0.23**
								RSD = 3%							**RSD = 6%**	**RSD = 4%**
2-Acc4	45	0	23.27	24.65	*6%*	49.69	33.07	0.67	1.42	1.34	*5%*	12.29	19.10	43%	0.50	0.25
	60	15	36.80	33.83	*8%*	81.66			2.08	2.14	*3%*	22.58			0.67	0.28
	80	35	57.85	54.11	*7%*	135.89	81.83	0.60	3.63	3.69	*2%*	39.78	47.25	17%	0.74	0.29
	100	55	95.55	90.66	*5%*	241.91	147.95	0.61	5.34	5.42	*2%*	90.56	85.42	6%	1.00	0.37
								μ = 0.63							**μ = 0.73**	**μ = 0.30**
								RSD = 5%							**RSD = 25%**	**RSD = 16%**
8-NA	50	0	7.30	7.04	*4%*	20.74	12.86	0.62	0.69	0.69	*1%*					
	70	20				25.30	16.51	0.65	0.86	0.87	*1%*					
	90	40	10.84	9.46	*14%*	33.80	19.50	0.58	1.22	1.32	*8%*					
	110	60	14.58	13.40	*8%*	39.09	22.11	0.57	1.43	1.42	*1%*					
	130	80	16.23	14.76	*9%*	61.37	40.34	0.66	2.18	2.28	*4%*					
								μ = 0.61								
								RSD = 6%								
8-CA	60	0	36.92	31.80	*15%*	56.88	30.20	0.53	1.14	1.12	*1%*					
	80	20	46.77	39.89	*16%*	81.15	39.14	0.48	1.59	1.63	*3%*					
	100	40	54.28	46.48	*15%*	107.95	54.28	0.50	1.89	1.92	*2%*					
	120	60	67.41	59.66	*12%*	134.15	69.16	0.52	2.48	2.65	*7%*					
	140	80	76.09	67.40	*12%*	176.57	98.19	0.56	3.25	3.39	*4%*					
								μ = 0.52								
								RSD = 5%								
all											**μ_{all} = 4%**				***μ_{all} = 0.59***	***μ_{all} = 0.30***
															RSD = 34%	**RSD = 16%**

* comparison between τ_0 obtained in PT and $\sigma_E/\sqrt{3}$ calculated from the CUCT results

Preprints (www.preprints.org) | NOT PEER-REVIEWED | Posted: 21 September 2021

References

[1] R.A. Buswell, W.R.L. da Silva, F.P. Bos, H.R. Schipper, D. Lowke, N. Hack, H. Kloft, V. Mechtcherine, T. Wangler, N. Roussel, A process classification framework for defining and describing Digital Fabrication with Concrete, Cem. Concr. Res. 134 (2020). https://doi.org/10.1016/j.cemconres.2020.106068.

[2] V. Mechtcherine, F.P. Bos, A. Perrot, W.R.L. da Silva, V.N. Nerella, S. Fataei, R.J.M. Wolfs, M. Sonebi, N. Roussel, Extrusion-based additive manufacturing with cement-based materials – Production steps, processes, and their underlying physics: A review, Cem. Concr. Res. 132 (2020) 106037. https://doi.org/10.1016/j.cemconres.2020.106037.

[3] V.N. Nerella, M. Krause, V. Mechtcherine, Direct printing test for buildability of 3D-printable concrete considering economic viability, Autom. Constr. 109 (2020) 102986. https://doi.org/10.1016/j.autcon.2019.102986.

[4] J. Kruger, Rheo-mechanics modelling of 3D concrete printing constructability, 2019. https://doi.org/10.13140/RG.2.2.16259.04649.

[5] A. Szabo, L. Reiter, E. Lloret-Fritschi, T. Wangler, F. Gramazio, M. Kohler, R.J. Flatt, ACDC: The Admixture Controlled Digital Casting and Its Application to Thin Folded Concrete Structures, in: F. Bos, S.S. Lucas, R.J.M. Wolfs, T.M. Salet (Eds.), Second RILEM Int. Conf. Concr. Digit. Fabr. DC 2020. RILEM Bookseries, Springer, Cham, 2020: pp. 956–966. https://doi.org/10.1007/978-3-030-49916-7_93.

[6] S. Hou, Z. Duan, J. Xiao, J. Ye, A review of 3D printed concrete: Performance requirements, testing measurements and mix design, Constr. Build. Mater. 273 (2021). https://doi.org/10.1016/j.conbuildmat.2020.121745.

[7] T. Wangler, N. Roussel, F.P. Bos, T.A.M. Salet, R.J. Flatt, Digital Concrete: A Review, Cem. Concr. Res. 123 (2019). https://doi.org/10.1016/j.cemconres.2019.105780.

[8] R.A. Buswell, W.R. Leal de Silva, S.Z. Jones, J. Dirrenberger, 3D printing using concrete extrusion: A roadmap for research, Cem. Concr. Res. 112 (2018) 37–49. https://doi.org/10.1016/j.cemconres.2018.05.006.

[9] Z. Li, M. Hojati, Z. Wu, J. Piasente, N. Ashrafi, J.P. Duarte, S. Nazarian, S.G. Bilén, A.M. Memari, A. Radlińska, Fresh and hardened properties of extrusion-based 3D-printed cementitious materials: A review, Sustainability. 12 (2020) 1–33. https://doi.org/10.3390/su12145628.

[10] T. Wangler, E. Lloret, L. Reiter, N. Hack, F. Gramazio, M. Kohler, M. Bernhard, B. Dillenburger, J. Buchli, N. Roussel, R. Flatt, Digital Concrete: Opportunities and Challenges, RILEM Tech. Lett. 1 (2016) 67. https://doi.org/10.21809/rilemtechlett.2016.16.

[11] F.P. Bos, P.J. Kruger, S.S. Lucas, G.P.A.G. van Zijl, Juxtaposing fresh material characterisation methods for buildability assessment of 3D printable cementitious mortars, Cem. Concr. Compos. 120 (2021) 104024. https://doi.org/10.1016/j.cemconcomp.2021.104024.

[12] I. Ivanova, V. Mechtcherine, Evaluation of Structural Build-Up Rate of Cementitious Materials by Means of Constant Shear Rate Test: Parameter Study, in: Rheol. Process. Constr. Mater. RILEM Bookseries B. Ser., 2020: pp. 209–218.

[13] Y. Qian, S. Kawashima, Use of creep recovery protocol to measure static yield stress and structural rebuilding of fresh cement pastes, Cem. Concr. Res. 90 (2016) 73–79. https://doi.org/10.1016/j.cemconres.2016.09.005.

[14] Q. Yuan, X. Lu, K.H. Khayat, D. Feys, C. Shi, Small amplitude oscillatory shear technique to evaluate structural build-up of cement paste, Mater. Struct. 50 (2017) 112. https://doi.org/10.1617/s11527-016-0978-2.

[15] I. Ivanova, V. Mechtcherine, Possibilities and challenges of constant shear rate test for evaluation of structural build-up rate of cementitious materials, Cem. Concr. Res. 130 (2020). https://doi.org/10.1016/j.cemconres.2020.105974.

[16] N. Roussel, G. Ovarlez, S. Garrault, C. Brumaud, The origins of thixotropy of fresh cement pastes, Cem. Concr. Res. 42 (2012) 148–157. https://doi.org/10.1016/j.cemconres.2011.09.004.

[17] N. Roussel, A thixotropy model for fresh fluid concretes: Theory, validation and applications, Cem. Concr. Res. 36 (2006) 1797–1806. https://doi.org/10.1016/j.cemconres.2006.05.025.

[18] A. Perrot, D. Rangeard, A. Pierre, Structural built-up of cement-based materials used for 3D-printing extrusion techniques, Mater. Struct. 49 (2016) 1213–1220. https://doi.org/10.1617/s11527-015-0571-0.

[19] B. Zhu, J. Pan, B. Nematollahi, Z. Zhou, Y. Zhang, J. Sanjayan, Development of 3D printable engineered cementitious composites with ultra-high tensile ductility for digital construction, Mater. Des. 181 (2019). https://doi.org/10.1016/j.matdes.2019.108088.

[20] T.T. Le, S.A. Austin, S. Lim, R.A. Buswell, A.G.F. Gibb, T. Thorpe, Mix design and fresh properties for high-performance printing concrete, Mater. Struct. 45 (2012) 1221–1232. https://doi.org/10.1617/s11527-012-9828-z.

[21] R.J.M. Wolfs, F.P. Bos, T.A.M. Salet, Triaxial compression testing on early age concrete for numerical analysis of 3D concrete printing, Cem. Concr. Compos. 104 (2019). https://doi.org/10.1016/j.cemconcomp.2019.103344.

[22] F.A. Bester, M. Van Den Heever, P.J. Kruger, S. Zeranka, G.P.A.G. Van Zijl, Benchmark structures for 3D concrete printing, Proc. Fib Symp. 2019 Concr. - Innov. Mater. Des. Struct. (2019) 305–312.

[23] Y. Weng, M. Li, M.J. Tan, S. Qian, Design 3D printing cementitious materials via Fuller Thompson theory and Marson-Percy model, Constr. Build. Mater. 163 (2018) 600–610. https://doi.org/10.1016/j.conbuildmat.2017.12.112.

[24] R.J.M. Wolfs, F.P. Bos, T.A.M. Salet, Early age mechanical behaviour of 3D printed concrete: Numerical modelling and experimental testing, Cem. Concr. Res. 106 (2018) 103–116. https://doi.org/10.1016/j.cemconres.2018.02.001.

[25] R. Jayathilakage, P. Rajeev, J. Sanjayan, Yield stress criteria to assess the buildability of 3D concrete printing, Constr. Build. Mater. 240 (2020). https://doi.org/10.1016/j.conbuildmat.2019.117989.

[26] S. Cho, J. Kruger, F. Bester, M. van den Heever, A. van Rooyen, G. van Zijl, A Compendious Rheo-Mechanical Test for Printability Assessment of 3D Printable Concrete, in: F. Bos, S.S. Lucas, R.J.M. Wolfs, T.M. Salet (Eds.), Second RILEM Int. Conf. Concr. Digit. Fabr. DC 2020. RILEM Bookseries, Springer, Cham, 2020: pp. 196–205. https://doi.org/10.1007/978-3-030-49916-7_20.

Preprints (www.preprints.org) | NOT PEER-REVIEWED | Posted: 21 September 2021

[27] J. Kruger, S. Zeranka, G. van Zijl, Quantifying Constructability Performance of 3D Concrete Printing via Rheology-Based Analytical Models, in: F. Bos, S.S. Lucas, R.J.M. Wolfs, T.M. Salet (Eds.), Second RILEM Int. Conf. Concr. Digit. Fabr. DC 2020. RILEM Bookseries, Springer, Cham, 2020: pp. 400–408. https://doi.org/10.1007/978-3-030-22566-7_46.

[28] C. Joh, J. Lee, T.Q. Bui, J. Park, I.-H. Yang, Buildability and Mechanical Properties of 3D Printed Concrete, Materials (Basel). 13 (2020). https://doi.org/10.3390/ma13214919.

[29] N. Roussel, Rheological requirements for printable concretes, Cem. Concr. Res. 112 (2018) 76–85. https://doi.org/10.1016/j.cemconres.2018.04.005.

[30] A. Perrot, D. Rangeard, A. Pierre, Structural built-up of cement-based materials used for 3D-printing extrusion techniques, Mater. Struct. 49 (2016) 1213–1220. https://doi.org/10.1617/s11527-015-0571-0.

[31] T. Wangler, E. Lloret, L. Reiter, N. Hack, F. Gramazio, M. Kohler, M. Bernhard, B. Dillenburger, J. Buchli, N. Roussel, R. Flatt, Digital Concrete: Opportunities and Challenges, RILEM Tech. Lett. 1 (2016). https://doi.org/10.21809/rilemtechlett.2016.16.

[32] B. Panda, J.H. Lim, M.J. Tan, Mechanical properties and deformation behaviour of early age concrete in the context of digital construction, Compos. Part B. 165 (2019) 563–571. https://doi.org/10.1016/j.compositesb.2019.02.040.

[33] S. Kurt, Y.A. Atalay, O.E. Aydın, B. Avcıoğlu, T. Yıldırım, G.B. Göktepe, S. Emir, Z.B. Bundur, H. Paksoy, Design of Energy-Efficient White Portland Cement Mortars for Digital Fabrication, in: F. Bos, S.S. Lucas, R. Wolfs, T.M. Salet (Eds.), Second RILEM Int. Conf. Concr. Digit. Fabr. DC 2020, Springer, Cham, 2020: pp. 64–72. https://doi.org/10.1007/978-3-030-49916-7_7.

[34] A. Kazemian, X. Yuan, E. Cochran, B. Khoshnevis, Cementitious materials for construction-scale 3D printing: Laboratory testing of fresh printing mixture, Constr. Build. Mater. 145 (2017) 639–647. https://doi.org/10.1016/j.conbuildmat.2017.04.015.

[35] L. Reiter, Structural Build-up for Digital Fabrication with Concrete - Materials, Methods and Processes, 2019. https://doi.org/10.3929/ethz-b-000456199.

[36] L. Casagrande, L. Esposito, C. Menna, D. Asprone, F. Auricchio, Effect of testing procedures on buildability properties of 3D-printable concrete, Constr. Build. Mater. 245 (2020). https://doi.org/10.1016/j.conbuildmat.2020.118286.

[37] B. Panda, S.C. Paul, L.J. Hui, Y.W.D. Tay, M.J. Tan, Additive manufacturing of geopolymer for sustainable built environment, J. Clean. Prod. 167 (2017) 281–288. https://doi.org/10.1016/j.jclepro.2017.08.165.

[38] R.J.M. Wolfs, F.P. Bos, T.A.M. Salet, Correlation between destructive compression tests and non-destructive ultrasonic measurements on early age 3D printed concrete, Constr. Build. Mater. 181 (2018) 447–454. https://doi.org/10.1016/j.conbuildmat.2018.06.060.

[39] L. Casagrande, L. Esposito, C. Menna, D. Asprone, F. Auricchio, Mechanical Characterization of Cement-Based Mortar Used in 3DCP Including Early-Age Creep Effects, in: F. Bos, S.S. Lucas, R.J.M. Wolfs, T.M. Salet (Eds.), Second RILEM Int. Conf. Concr. Digit. Fabr. DC 2020. RILEM Bookseries, Springer, Cham, 2020: pp. 407–416. https://doi.org/10.1007/978-3-030-49916-7_42.

[40] U. Pott, D. Stephan, Penetration test as a fast method to determine yield stress and structural build-up for 3D printing of cementitious materials, Cem. Concr. Compos. 121 (2021) 104066. https://doi.org/10.1016/j.cemconcomp.2021.104066.

[41] D. Feys, K.H. Khayat, Particle migration during concrete rheometry: How bad is it?, Mater. Struct. 50 (2017). https://doi.org/10.1617/s11527-016-0992-4.

[42] A. Benamara, A. Pierre, A. Kaci, Y. Melinge, 3D Printing of a Cement-Based Mortar in a Complex Fluid Suspension: Analytical Modeling and Experimental Tests, in: F. Bos, S.S. Lucas, R. Wolfs, T.M. Salet (Eds.), Second RILEM Int. Conf. Concr. Digit. Fabr. DC 2020. RILEM Bookseries, Springer, Cham, 2020: pp. 768–777. https://doi.org/10.1007/978-3-030-49916-7_76.

[43] D. Lootens, P. Jousset, L. Martinie, N. Roussel, R.J. Flatt, Yield stress during setting of cement pastes from penetration tests, Cem. Concr. Res. 39 (2009) 401–408. https://doi.org/10.1016/j.cemconres.2009.01.012.

[44] U. Pott, C. Ehm, C. Jakob, D. Stephan, Investigation of the Early Cement Hydration with a New Penetration Test, Rheometry and In-Situ XRD, in: V. Mechtcherine, K. Khayat, E. Secrieru (Eds.), Rheol. Process. Constr. Mater., Springer International Publishing, Cham, 2020: pp. 246–255.

[45] I. Dressler, N. Freund, D. Lowke, The Effect of Accelerator Dosage on Fresh Concrete Properties and on Interlayer Strength in Shotcrete 3D Printing, Materials (Basel). 13 (2020). https://doi.org/10.3390/ma13020374.

[46] I. Dressler, N. Freund, D. Lowke, Control of Strand Properties Produced with Shotcrete 3D Printing by Accelerator Dosage and Process Parameters, Springer, Cham, 2020. https://doi.org/10.1007/978-3-030-49916-7_5.

[47] Y. Jacquet, V. Picandet, D. Rangeard, A. Perrot, Gravity Driven Tests to Assess Mechanical Properties of Printable Cement-Based Materials at Fresh State, in: F. Bos, S.S. Lucas, R.J.M. Wolfs, T.M. Salet (Eds.), Second RILEM Int. Conf. Concr. Digit. Fabr. DC 2020. RILEM Bookseries, Springer, Cham, 2020: pp. 280–289. https://doi.org/10.1007/978-3-030-49916-7_29.

[48] J. Kruger, S. Zeranka, G. van Zijl, A rheology-based quasi-static shape retention model for digitally fabricated concrete, Constr. Build. Mater. 254 (2020). https://doi.org/10.1016/j.conbuildmat.2020.119241.

[49] A.S.J. Suiker, R.J.M. Wolfs, S.M. Lucas, T.A.M. Salet, Elastic buckling and plastic collapse during 3D concrete printing, Cem. Concr. Res. 135 (2020) 106016. https://doi.org/10.1016/j.cemconres.2020.106016.

[50] V.N. Nerella, Development and characterisation of cement-based materials for extrusion-based 3D-printing, Technische Universität Dresden, 2019. https://tud.qucosa.de/landing-page/?tx_dlf[id]=https%3A%2F%2Ftud.qucosa.de%2Fapi%2Fqucosa%253A37706%2Fmets.

[51] EN 1015-3:2007 Methods Of Test For Mortar For Masonry - Part 3: Determination Of Consistence Of Fresh Mortar (By

Preprints (www.preprints.org) | NOT PEER-REVIEWED | Posted: 21 September 2021

Flow Table), German Institute for Standardisation (Deutsches Institut für Normung), 2007.
[52] DIN EN 12350-6 Testing fresh concrete - Part 6: Density, n.d.
[53] A.R. Arunothayan, B. Nematollahi, J. Sanjayan, R. Ranade, S.H. Bong, K. Khayat, Quantitative Evaluation of Orientation of Steel Fibers in 3D-Printed Ultra-High Performance Concrete, in: F. Bos, S.S. Lucas, R.J.M. Wolfs, T.M. Salet (Eds.), Second RILEM Int. Conf. Concr. Digit. Fabr. DC 2020. RILEM Bookseries, Springer, Cham, 2020: pp. 389–397. https://doi.org/10.1007/978-3-030-49916-7_40.
[54] M. Hambach, D. Volkmer, Properties of 3D-printed fiber-reinforced Portland cement paste, Cem. Concr. Compos. 79 (2017) 62–70. https://doi.org/10.1016/j.cemconcomp.2017.02.001.
[55] J. Reinold, V.N. Nerella, V. Mechtcherine, G. Meschke, Extrusion process simulation and layer shape prediction during 3D-concrete-printing using the Particle Finite Element Method, Preprints. (2020) 1–25. https://doi.org/10.20944/preprints202007.0715.v1.